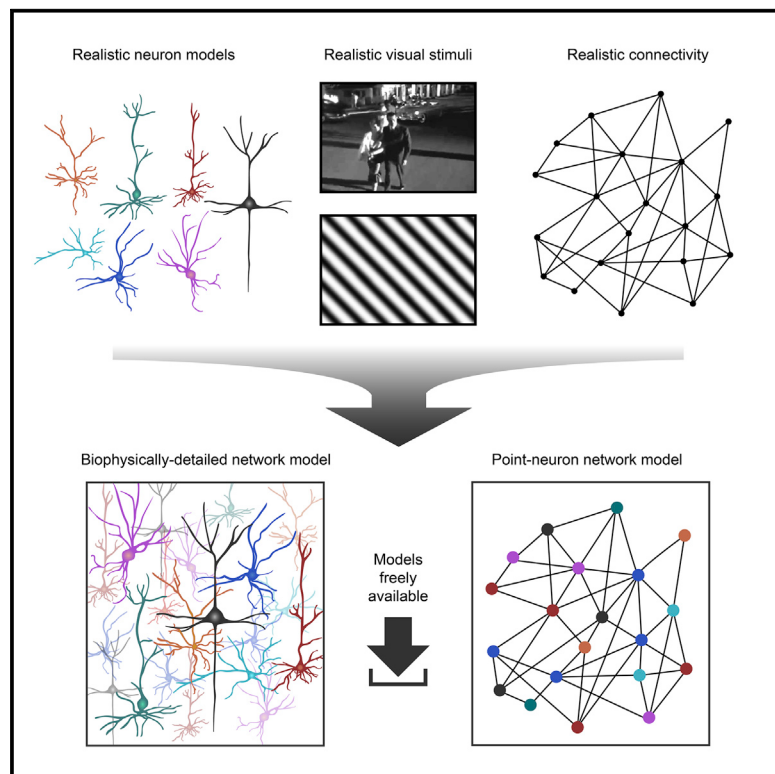


Systematic Integration of Structural and Functional Data into Multi-scale Models of Mouse Primary Visual Cortex

Graphical Abstract



Authors

Yazan N. Billeh, Binghuang Cai,
Sergey L. Gratiy, ..., Christof Koch,
Stefan Mihalas, Anton Arkhipov

Correspondence

yazanb@alleninstitute.org (Y.N.B.),
antona@alleninstitute.org (A.A.)

In Brief

Billeh et al. systematically integrate multi-modal data about neuron types, connectivity, and sensory innervations to create biologically realistic models of the mouse primary visual cortex at two levels of resolution, shared freely as a community resource.

Highlights

- Two network models of the mouse primary visual cortex are developed and released
- One uses compartmental-neuron models and the other point-neuron models
- The models recapitulate observations from *in vivo* experimental data
- Simulations identify experimentally testable predictions about cortex circuitry



NeuroResource

Systematic Integration of Structural and Functional Data into Multi-scale Models of Mouse Primary Visual Cortex

Yazan N. Billeh,^{1,*} Binghuang Cai,¹ Sergey L. Gratiy,¹ Kael Dai,¹ Ramakrishnan Iyer,¹ Nathan W. Gouwens,¹ Reza Abbasi-Asl,^{1,2} Xiaoxuan Jia,¹ Joshua H. Siegle,¹ Shawn R. Olsen,¹ Christof Koch,¹ Stefan Mihalas,¹ and Anton Arkhipov^{1,3,*}

¹Allen Institute for Brain Science, Seattle, WA, USA

²UCSF Weill Institute for Neurosciences, Department of Neurology, University of California, San Francisco, CA, USA

³Lead Contact

*Correspondence: yazanb@alleninstitute.org (Y.N.B.), antona@alleninstitute.org (A.A.)

<https://doi.org/10.1016/j.neuron.2020.01.040>

SUMMARY

Structural rules underlying functional properties of cortical circuits are poorly understood. To explore these rules systematically, we integrated information from extensive literature curation and large-scale experimental surveys into a data-driven, biologically realistic simulation of the awake mouse primary visual cortex. The model was constructed at two levels of granularity, using either biophysically detailed or point neurons. Both variants have identical network connectivity and were compared to each other and to experimental recordings of visual-driven neural activity. While tuning these networks to recapitulate experimental data, we identified rules governing cell-class-specific connectivity and synaptic strengths. These structural constraints constitute hypotheses that can be tested experimentally. Despite their distinct single-cell abstraction, both spatially extended and point models perform similarly at the level of firing rate distributions for the questions we investigated. All data and models are freely available as a resource for the community.

INTRODUCTION

Mechanisms connecting the structure of cortical circuits to patterns of neural activity are poorly understood. Elucidating such mechanisms requires systematic data collection and modeling to “understand” these data. Such an understanding is always relative to a particular domain of interest—be it modeling the physics of excitable brain tissue (Koch, 1999; Einevoll et al., 2013), mimicking the computations that lead to a particular set of firing rates (Yamins and DiCarlo, 2016), or diagnosing and ultimately curing psychiatric and neurological diseases. The first option—biologically realistic modeling—appears necessary to disentangle the extreme complexity of cortex (Harris and Mrsic-Flogel, 2013; Harris and Shepherd, 2015; Amunts et al., 2016; Koch and Jones, 2016; Martin and Chun, 2016; Chevée and Brown, 2018; Einevoll et al., 2019).

Simulating cortical circuits has a long history (e.g., Wehmeier et al., 1989; Zemel and Sejnowski, 1998; Troyer et al., 1998; Kruckowski and Miller, 2001; Traub et al., 2005; Zhu et al., 2009; Reimann et al., 2013; Potjans and Diesmann, 2014; Markram et al., 2015; Arkhipov et al., 2018; Joglekar et al., 2018; Schmidt et al., 2018; Antolík et al., 2019; Schwalger and Chizhov, 2019), with models incrementally building upon their predecessors. The simulations described here are a further instance of this evolution toward digital simulacra that predict new experi-

ments, are insightful, and are ever more faithful to the vast complexity of cortical cell classes, connections, and activity.

We developed data-driven models of the mouse primary visual cortex (area V1), containing ~230,000 neurons, to simulate physiological studies with arbitrary visual stimuli (Figure 1A). We focus on mouse V1 due to substantial amounts of high-quality data, especially from standardized pipelines at the Allen Institute for Brain Science. However, our primary aim is to provide a computational platform to study cortical structure and computation in general, under realistic biological constraints. Our models can be used as templates for other cortical areas. We developed two variants: using biophysically detailed compartmental neuronal models (Gouwens et al., 2018) or generalized leaky integrate and fire (GLIF) point-neuron models (Teeter et al., 2018), both constrained by experimental measurements and reproducing multiple observations from our electrical recordings *in vivo* (Siegle et al., 2019). Users of our resources should select the model based on the question of interest, where, for instance, investigating local field potentials, dendritic integration, or local learning rules clearly requires using biophysical resolution with spatially extended dendrites.

We describe three predictions that emerged in the process of building and testing these models. First, the strength (but not the probability) of synaptic connections from excitatory to non-parvalbumin (Pvalb) inhibitory neurons is determined by how similarly tuned pre- and post-synaptic neurons are to sensory stimuli.



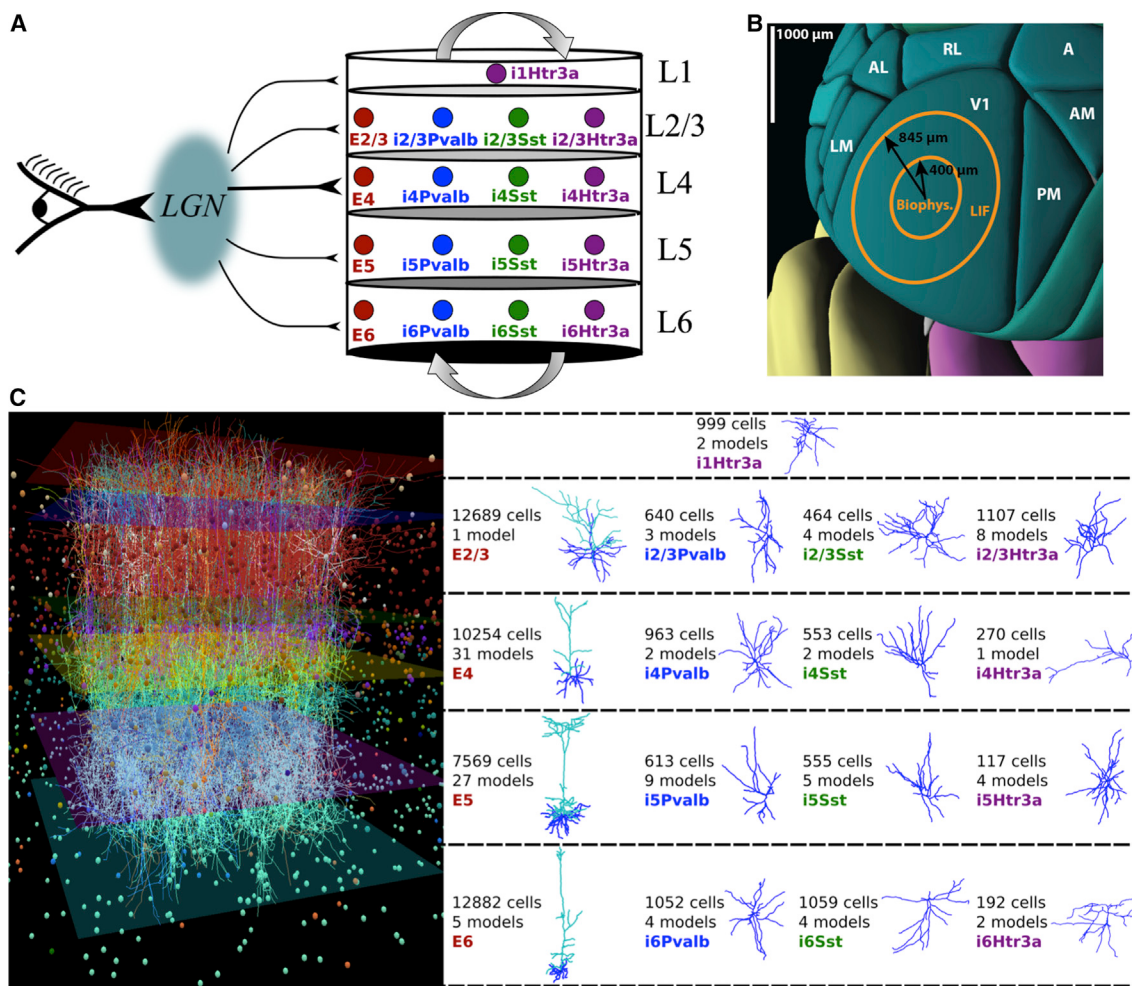


Figure 1. Overview of V1 Models

(A) Both models consist of one excitatory and three inhibitory classes (Pvalb, Sst, and Htr3a) in L2/3 to L6; L1 has but a single, inhibitory Htr3a class. Visual stimuli are conveyed by projections from the LGN (Figures 2 and 3).

(B) Mouse posterior cortex, illustrating the region covered by the models (400-μm radius for the core; 845-μm radius with surrounding annulus).

(C) Left: visualization of the biophysically detailed network (1% of neurons shown). Right: exemplary dendritic morphologies for each class are shown. The total number of neurons and number of unique models in every class are indicated.

Second, the synaptic strength in connected pairs of excitatory neurons depends on both the similarity of the stimulus tuning of the two neurons and the similarity in the phase of their responses. Third, as a consequence of the anisotropic mapping from visual to cortical space (e.g., a 10° movement in the visual space requires ~250 μm movement within cortex for elevation but only ~140 μm for azimuth; Schuett et al., 2002; Kalatsky and Stryker, 2003), there is an asymmetry between neurons preferring vertical versus horizontal directions of motion that is compensated for by an asymmetric circuit architecture.

Our models use the Brain Modeling ToolKit (BMTK) (<https://alleninstitute.github.io/bmtk>; Gratiy et al., 2018) that facilitates simulations with both NEURON (Hines and Carnevale, 1997) and NEST (Gewaltig and Diesmann, 2007) and supports Python 2.7 and 3.6. Model and simulation outputs are saved in the SONATA format (<https://github.com/AllenInstitute/sonata>; Dai et al., 2020). All models, code, and meta-data are publicly avail-

able via our web portal at <https://portal.brain-map.org/explore/models/mv1-all-layers>. Tutorials for BMTK and our models are available online and presented in the **Getting Started** section of the **STAR Methods**. As an open public resource, these models can predict and complement other experimental and modeling endeavors. The *in vivo* extracellular recordings used for comparison are recorded from a standardized pipeline that is also freely available (Siegle et al., 2019; <https://portal.brain-map.org/explore/circuits/visual-coding-neuropixels>).

RESULTS

Representing Diverse Cortical Cell Classes

Our biophysical and GLIF model variants use the same connectivity graph (i.e., each neuron in one variant has an exact counterpart in the other, with the same coordinates, presynaptic sources, and post-synaptic targets). The first step in building this

network is to instantiate an 845- μm radius of cortex (Figure 1B). For the biophysically detailed variant, the “core” (400- μm radius) is composed of morphologically derived multi-compartmental neurons with somatic Hodgkin-Huxley dynamics and passive dendrites (Gouwens et al., 2018), surrounded by an annulus of leaky-integrate-and-fire neurons, to avoid boundary artifacts (Arkhipov et al., 2018). We here focus on the network within this central core.

Neuron models are reconstructed from slice electrophysiology (Gouwens et al., 2018; Teeter et al., 2018; <http://celltypes.brain-map.org>). Although recent surveys suggest ~50–100 classes in V1 (Tasic et al., 2018; Gouwens et al., 2019), the currently available neuronal models, connectivity data, and *in vivo* recordings offer lower cell class resolution into 17 classes (Figures 1A and 1C). Inhibitory neuron classes are Htr3a in layer 1 (L1) and Pvalb, somatostatin (Sst), and Htr3a in L2/3 to L6 (Lee et al., 2010; Tremblay et al., 2016). Note that VIP interneurons are a subclass of Htr3a in L2/3–L6; because they are studied most extensively among Htr3a neurons, we resort to using VIP studies to constrain the Htr3a class. One class of excitatory neurons is each present in L2/3 to L6 (E2/3, E4, E5, and E6). These 17 cell classes are represented by 112 unique individual models for the biophysical and 111 for the GLIF network. Cell densities across layers are estimated from anatomical data (Schüz and Palm, 1989; Lee et al., 2010), with an 85%:15% fraction for excitatory and inhibitory neurons (see STAR Methods). The final networks contain 230,924 cells (51,978 in the core).

We determined synaptic connectivity using three design iterations. In the first (see immediately below), we constructed the feedforward geniculate input into cortex. Second, we introduced massive synaptic recurrency, which depended on the stimulus tuning of the cells. Finally, we refined the recurrent connectivity with respect to the stimulus tuning properties.

Thalamic Input to the V1 Models

The lateral geniculate nucleus (LGN) of the thalamus mediates retinal input to V1. We created an LGN module that generates action potentials for arbitrary visual stimuli (see Getting Started in STAR Methods).

Creating LGN Units

The LGN module is composed of spatiotemporally separable filters (released publicly via BMTK; <https://alleninstitute.github.io/bmtk>) fitted to electrophysiology recordings from mouse LGN (Durand et al., 2016). In a substantial elaboration over our previous work (Arkhipov et al., 2018), we developed filters for four classes of experimentally observed functional responses (Pispolo et al., 2013; Durand et al., 2016): sustained ON; sustained OFF; transient OFF; and ON/OFF, further subdivided according to preferred temporal frequency (TF) (Figure 2A; Table 1 in STAR Methods). We average the experimentally recorded responses for each class to create filters that can process any spatiotemporal input and compute a firing rate/spike train output (Figure 2B; STAR Methods). The filters are distributed in visual space according to occurrence ratios of the LGN cell classes (Durand et al., 2016).

Direction Selective Input into V1 Cells

Our main emphasis is on relating the structure of cortical circuits to their *in vivo* function. We sought to recapitulate physiological levels of direction selectivity (Niell and Stryker, 2008; Durand

et al., 2016) and, in doing so, study the underlying structure of feedforward thalamocortical inputs and recurrent connectivity (our freely available models permit testing of many other metrics).

Because recent work indicates that direction selectivity is produced in V1 from convergence of spatiotemporally asymmetric LGN inputs (Lien and Scanziani, 2018), we assume that LGN innervation into V1 neurons contains a slow (sustained) subfield and a fast (transient) subfield (Figure 2C). These produce an asymmetry in responses to opposite directions of motion (Figure 2D). A simplified theoretical description (see STAR Methods; Figure S1) suggests sufficiently high orientation selectivity indices (OSIs) and direction selectivity indices (DSIs) with such subfields (Lien and Scanziani, 2013, 2018) as well as reversal of the preferred direction as the spatial frequency of grating increases (analogous to aliasing in the fly visual system; van Santen and Sperling, 1984; Borst and Egelhaaf, 1989; Arenz et al., 2017), which we confirmed experimentally (Billeh et al., 2019).

Creating and Testing Thalamocortical Connectivity

We instantiated 17,400 LGN filters in visual space (Figure 2A) and established LGN-to-V1 connections using the following three-step procedure (see STAR Methods).

The first step selects the LGN units projecting to each V1 neuron utilizing the spatiotemporally asymmetric architecture that yields direction and orientation selectivity (Lien and Scanziani, 2013, 2018) and selectively innervating only excitatory and Pvalb neurons in L2/3–L6 and non-Pvalb neurons in L1 (Kloc and Maffei, 2014; Ji et al., 2016). For each V1 neuron, we determined the visual center, size, and directionality (a pre-assigned preferred angle of stimulus motion) of elliptical subfields from which LGN filters will be sampled (Figure 3A; Table 2 in STAR Methods). We then identified LGN receptive fields (RFs) (parameterized during filter construction) that overlap with these elliptical subfields of the V1 neuron. One subfield always samples from transient OFF LGN filters and the other from sustained ON or OFF (see STAR Methods).

The second step (for the biophysical model only, see STAR Methods) determines the number and placement of synapses on V1 neurons, using data on LGN axonal density (Morgenstern et al., 2016) and estimates of synapse numbers per neuron (Schoonover et al., 2014; Bopp et al., 2017). The effect of dendritic placement on the somatic charge is shown in Figure S1.

The third and final step establishes the strength of the thalamocortical synapses based on experimental current measurements (Lien and Scanziani, 2013; Ji et al., 2016). The strength is scaled to match the target mean current (Figures 3B and 3C) in response to a drifting grating (see STAR Methods). Layer 4 is the main target of the thalamocortical projections, and therefore, the currents are largest in this layer (Figures 3B and 3C).

To test the outcome of this procedure, we simulated the network without recurrent connections using drifting gratings. Individual neurons are direction selective (Figure 3D), consistent with experimental measurements of LGN input currents (Lien and Scanziani, 2013, 2018). At the network level (example raster in Figure 3E), the average firing rates, DSIs, and OSIs due to LGN-only input are calculated (Figures 3F, 3G, and S2, respectively). For reference, data from *in vivo* extracellular Neuropixels recordings from awake mice (Siegle et al., 2019)

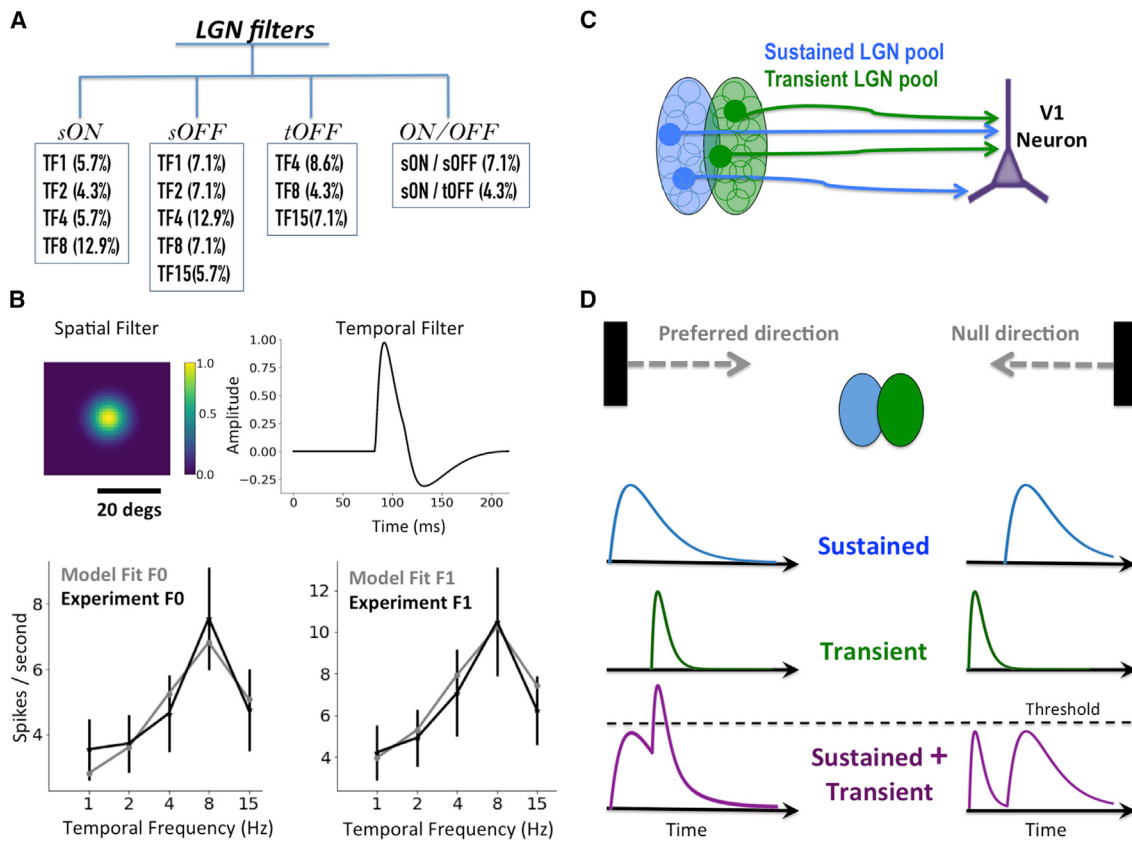


Figure 2. Filter Models of the Lateral Geniculate Nucleus (LGN)

(A) LGN cell classes fit from electrophysiological recordings (Durand et al., 2016) using spatiotemporally separable filters. Rate of occurrence of each class in our model is indicated.

(B) Example filter for the sON-TF8 class. Top: the spatial and temporal components of the filter are shown. Bottom: the F0 (cycle averaged mean rate response) and F1 (modulation of the response at the input stimulus frequency) components for the data and model fit in response to drifting gratings (mean \pm SEM).

(C) Schematic of a candidate pool of LGN cells, separated into sustained and transient subfields, projecting to a V1 cell with matching retinotopic positions.

(D) Schematic illustrating the direction selectivity mechanism. When a bar moves from left to right (preferred), the responses from both subfields overlap and exceed a threshold; no overlap occurs for movement in the opposite direction.

are included in Figure 3F (<https://portal.brain-map.org/explore/circuits/visual-coding-neuropixels>; Figure S2) and are used throughout the manuscript as a benchmark. Note that experimental data are robustly classified into regular-spiking (RS) and fast-spiking groups (FS), roughly corresponding to excitatory and Pvalb inhibitory neurons (small contributions from non-Pvalb inhibitory neurons are likely present in both groups). Hence, throughout the Results section, we compare model excitatory and Pvalb neurons with RS and FS cells, respectively.

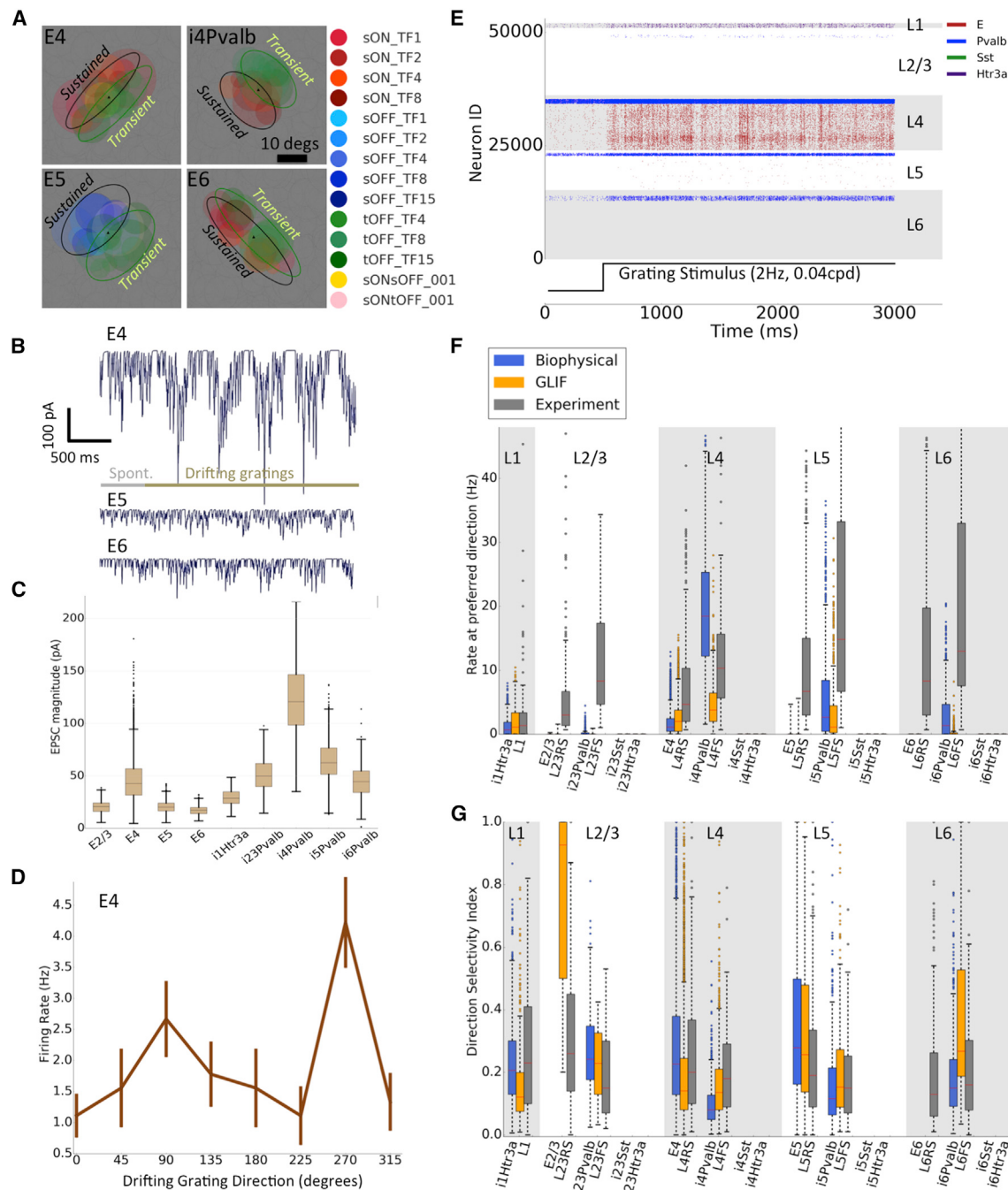
We define a similarity score, S , between distributions of a metric of interest to compare the experiments and models (one minus the Kolmogorov-Smirnov distance; see STAR Methods). If two distributions are identical, $S = 1$; $S \approx 0$ indicates quite different distributions (Figure S2). As expected, in the absence of intra-cortical amplification, S is low for firing rates (E-biophysical = 0.18; E-GLIF = 0.19; Pvalb-biophysical = 0.63; Pvalb-GLIF = 0.37), OSIs (E-biophysical = 0.22; E-GLIF = 0.22; Pvalb-biophysical = 0.60; Pvalb-GLIF = 0.54), and DSIs (E-biophysical = 0.22; E-GLIF = 0.21; Pvalb-biophysical = 0.73;

Pvalb-GLIF = 0.54). The biophysical and GLIF models compare well to one another (e.g., S values: E-rates = 0.96; E-OSI = 0.95; E-DSI = 0.95).

Finally, a background pool, mimicking the influence of the rest of the brain, provides input from a single Poisson source firing at a constant rate of 1 kHz to all V1 cells. The weights of this background were adjusted with the recurrent connectivity in place to ensure that the baseline firing rates of all neurons match experiments (see below).

Creating the Recurrent Connectivity in the V1 Network

Cortical circuits feature extensive recurrent connections that amplify thalamocortical inputs and shape cortical computations (Douglas et al., 1989, 1995; Douglas and Martin, 2007; Lien and Scanziani, 2013; Arkhipov et al., 2018). Despite many studies (e.g., Cauli et al., 1997; Dantzker and Callaway, 2000; Beierlein and Connors, 2002; Thomson et al., 2002; Beierlein et al., 2003; Mercer et al., 2005; Song et al., 2005; West et al., 2006; Yoshimura et al., 2005; Lefort et al., 2009; Hofer et al., 2011; Ko et al., 2011; Levy and Reyes, 2012; Olsen et al., 2012; Pfeffer

**Figure 3. Thalamic Inputs to Cortex**

(A) LGN filters connecting to four different V1 neurons. Black triangles and colored circles indicate the centers of the receptive fields of V1 and presynaptic LGN neurons. Gray circles indicate all other LGN filters. The elliptical subfields used to select the projecting LGN filters are shown.

(B–G) Responses of the biophysical V1 model to LGN input without any intracortical connections or background activity.

(B) Post-synaptic currents in V1 neurons responding to 500 ms of gray screen followed by a drifting grating.

(C) Summary of post-synaptic currents for every neuron class (for preferred drifting grating), after matching to target values (bar: median; box: 25th–75th percentile; whiskers: up to 1.5 of the interquartile range).

(D) Example tuning curve of a single E4 neuron (mean ± SEM across 10 trials).

(E) Example raster plot, same stimulus as in (B). Neuron classes with large excitatory postsynaptic current (EPSC) current values (boxplots in C) exhibit substantial spiking activity.

(legend continued on next page)

et al., 2013; Vélez-Fort et al., 2014; Bortone et al., 2014; Cossell et al., 2015; Jiang et al., 2015), data on the exact patterns and magnitude of V1 recurrent connectivity remain sparse. We set out to construct recurrent connections in a data-driven manner via extensive curation of the literature supplemented by Allen Institute data (Seeman et al., 2018) when available. This resulted in four key resources (Figure 4) containing estimates of (1) connection probability, (2) synaptic strengths, (3) axonal delays, and (4) dendritic targeting of synapses (freely available at <https://portal.brain-map.org/explore/models/mv1-all-layers>). Our cortical network contains specific instantiations of these connectivity rules. Unfortunately, there are no data for many connection classes in mouse V1; therefore, we used other sources of information in the following order of preference: mouse visual cortex; mouse non-visual or rat visual cortex; and rat non-visual cortex. Additional entries were filled using assumptions of similarity or the rat somatosensory cortex model (Markram et al., 2015; Reimann et al., 2015). 89 out of 289 entries remained undetermined (empty cells in Figures 4A and 4B) and were set to zero due to lack of data (see STAR Methods).

Figure 4A reports connection probabilities at 75 μm planar intersomatic distance, used as parameters for Gaussian distance-dependent connectivity rules for different source-target class pairs (Figure 4C). Excitatory-to-excitatory (E-to-E) connections in L2/3 of mouse V1 also exhibit “like-to-like” preferences (Ko et al., 2011; Cossell et al., 2015; Wertz et al., 2015; Lee et al., 2016), i.e., cells preferring similar stimuli are preferentially connected. We assume that such like-to-like rules are ubiquitous among E-to-E connections within and across layers (Figure 4D; see STAR Methods) but do not apply to E-to-I, I-to-E, and I-to-I connection probabilities, following experimental observations (Bock et al., 2011; Fino and Yuste, 2011; Packer and Yuste, 2011; Znamenskiy et al., 2018).

Recent experiments indicate that, besides connection probability, the amplitude (strength) of E-to-E synaptic connections in L2/3 also exhibits a like-to-like dependence (Cossell et al., 2015; Lee et al., 2016), which may be more important for neuronal tuning than connection probability rules (Schaub et al., 2015; Arkhipov et al., 2018). A similar like-to-like rule for synaptic strength (but not connection probability) has been reported for I-to-E connections (Znamenskiy et al., 2018). Thus, we assume that all synaptic strength classes (Figure 4B) are modulated by such a rule (Figure 4D). At this point, all like-to-like connection probability and synaptic strength profiles were symmetric with respect to the opposite preferred directions (Figure 4D).

Notably, experiments show that the Sst and Htr3a classes receive little to no LGN input (Figure 3; Ji et al., 2016) yet exhibit orientation and direction tuning (Liu et al., 2009; Kerlin et al., 2010; Ma et al., 2010). We assumed that this is due to like-to-like inputs from excitatory neurons. Indeed, our simulations implementing these rules exhibit substantial orientation and direction selectivity for Sst and Htr3a classes. We confirm this prediction by removing the like-to-like synaptic weight rule to Sst and

Htr3a neurons in our final model: indeed, both cell classes lose their orientation and direction selectivity properties (see below).

The third resource contains synaptic delays between different neuronal classes. Because measurements of these properties were particularly sparse, our final table is of coarser resolution (Figure 4E). The fourth resource (for the biophysical model) is a set of dendritic targeting rules for each connection class (Figure 4F). Experimental data for this are only available for a relatively small number of scenarios, and we used what were available from internal data and the literature (see STAR Methods).

Optimization of Synaptic Weights

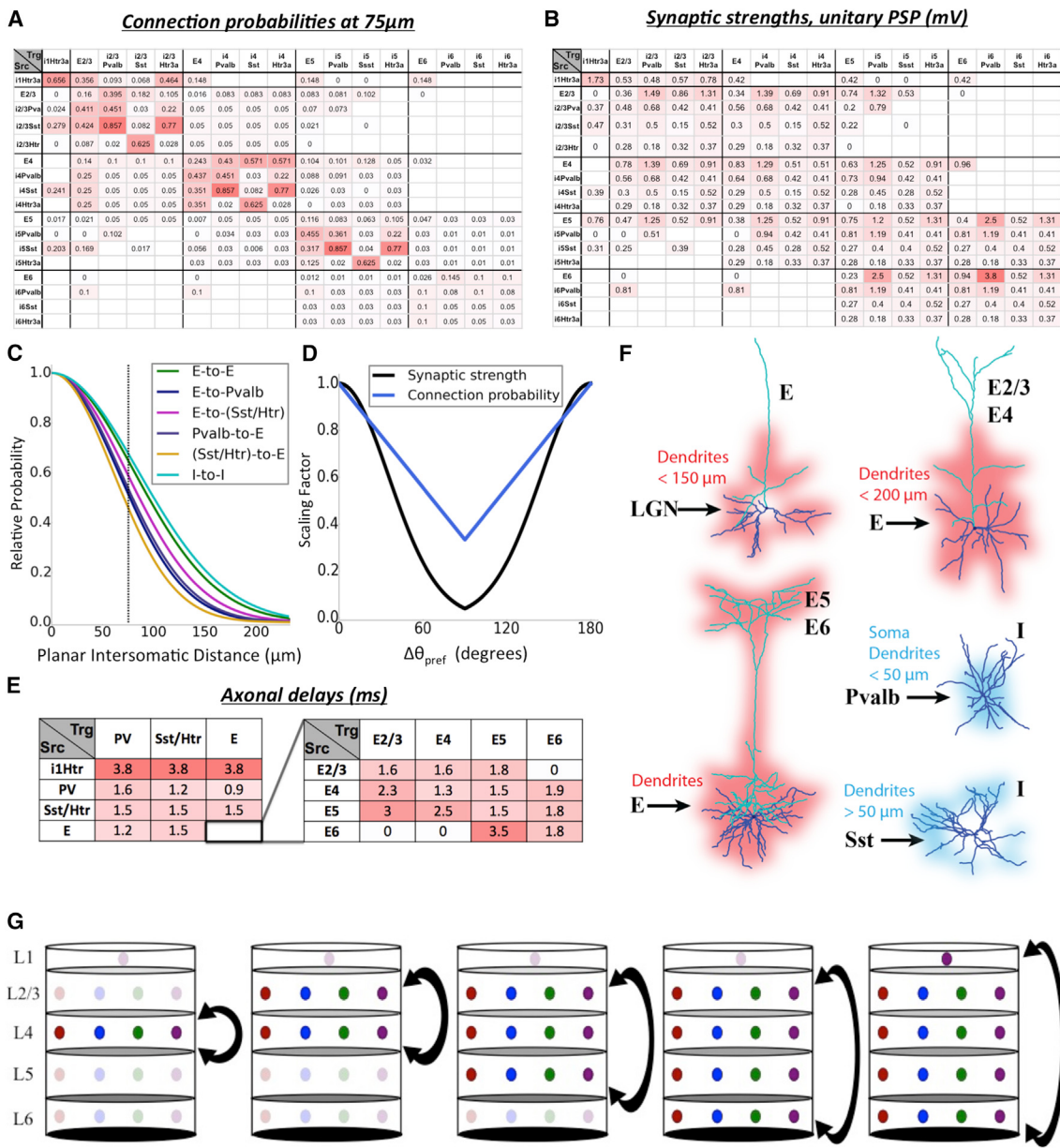
Although efficient optimization methods for recurrent spiking networks exist (e.g., Sussillo and Abbott, 2009; Nicola and Clopath, 2017), their performance has not yet achieved the level required for computationally expensive and highly heterogeneous networks as ours. We therefore use a heuristic optimization approach with three identical criteria applied to biophysical and GLIF networks: both (1) spontaneous firing rates as well as (2) peak firing rates in response to a single trial of a drifting grating (0.5 s long) should match experimental data, and (3) the models should not exhibit epileptic activity. The optimization applied to synaptic weights only via grid searches along weights of connections between neuronal classes, using uniform scaling of the selected weight class. The LGN-to-L4 weights were fixed, as they were matched directly to experimental recordings *in vivo* (Lien and Scanziani, 2013; Figure 3), whereas the net current inputs from LGN to other layers could vary because experimental data for those were obtained *in vitro* (Ji et al., 2016). Optimizing the full network in one step was very challenging; instead, we followed a stepwise, layer-by-layer procedure (Figures 4G and S3). We first optimized the recurrent weights within L4 and then added L2/3 recurrent connections and optimized the weights in both L4 and L2/3. This approach was repeated by adding L5, then L6, and finally L1 (Figures 4G and S3; see STAR Methods for details).

After optimization, a typical response to a drifting grating exhibits irregular activity (Figure 5A). The firing rates are similar to those measured *in vivo* (Figure 5B; S values: E-biophysical = 0.85; E-GLIF = 0.76; Pvalb-biophysical = 0.78; Pvalb-GLIF = 0.83). The OSIs are improved relative to LGN-only simulations (Figure 3G) yet still unsatisfactory (Figure S4; S values: E-biophysical = 0.56; E-GLIF = 0.64; Pvalb-biophysical = 0.37; Pvalb-GLIF = 0.60), and DSI is also poor (Figures 5C and 5D; S values: E-biophysical 0.65; E-GLIF = 0.69; Pvalb-biophysical = 0.43; Pvalb-GLIF = 0.59). The models match well with experimental data for signal and noise correlations (Figure S4; see STAR Methods). Again, both model variants are similar to each other (see Discussion; S values: E-rates = 0.86; E-OSI = 0.90; E-DSI = 0.91).

Although this is an improvement relative to LGN-only simulations (Figure 3), both models fail at orientation and direction selectivity. Although the structure of our network was

(F) Summary of firing rates. For reference, experimental data from *in vivo* extracellular electrophysiology recordings from awake mice (i.e., fully connected cortical circuit) are shown.

(G) Direction selectivity index (DSI) from responsive neurons. Some DSI values are high, as these simulations are purely feedforward and thus exhibit low firing rates.

**Figure 4. Recurrent Connectivity Rules**

- (A) Probability of connection at an intersomatic distance of 75 μ m.
- (B) Strength of connections (somatic unitary post-synaptic potential [PSP]).
- (C) The distance-dependent connection probabilities for different classes of connections.
- (D) The functional rules for connection probability (applied only to E-to-E connections) and synaptic strengths (applied to all connection classes) as a function of the difference in preferred direction angle θ_{pref} between the source and target neurons.
- (E) Axonal delays for connections between classes.
- (F) Dendritic targeting rules (see STAR Methods).
- (G) Schematic illustrating the layer-by-layer optimization procedure after incorporating all known data for recurrent connections. In the first stage, all recurrent connections except those within L4 were set to zero; L4 weights were optimized. Then, L2/3 connections (within layer and between L2/3 and L4) were added and optimized. The procedure was repeated, adding one layer at a time, until all layers were connected and optimized. See intermediate simulation outputs in Figure S3.

constrained by data relatively well at the level of cell classes, existing data provide much fewer constraints on the functional rules of individual recurrent connections, which relate tuning of

neurons to their connectivity and synaptic properties. We therefore reasoned that these functional rules require adjustment in the models.

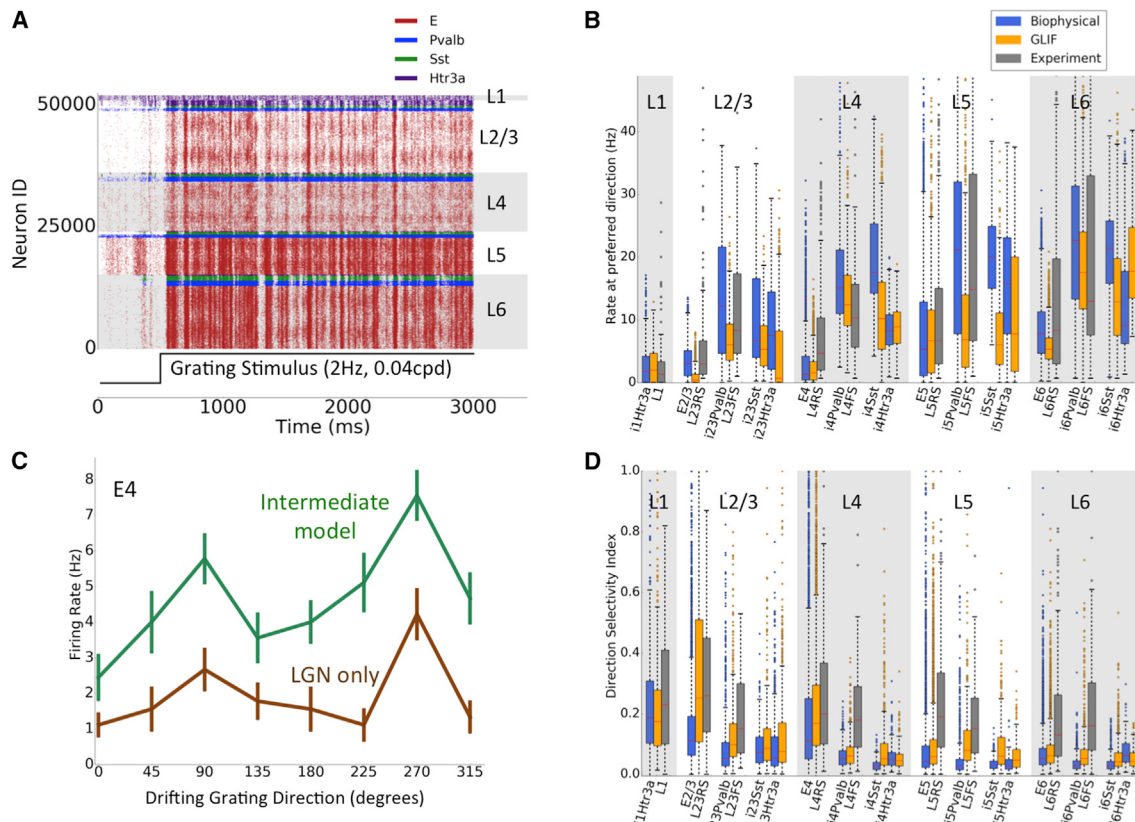


Figure 5. Initial Simulation Results from the Recurrent V1 Models

(A) Raster plot in response to a drifting grating (biophysical model). Within each cell class, the cell IDs are sorted according to the cells' preferred angles.

(B) Peak firing rates.

(C) Example tuning curves (mean \pm SEM across 10 trials) for an E4 neuron for both the intermediate model and LGN-only model (same neuron as Figure 3D).

(D) DSI for both models and *in vivo* measurements.

Refined Synaptic Functional Connections Amplify Direction Selectivity

Up to this point, the recurrent like-to-like connectivity rules in our models for probability and weights were symmetric with respect to $\Delta\theta = 90^\circ$, where $\Delta\theta$ is the difference between the preferred angles of the two neurons (Figure 4D). In other words, two neurons that prefer opposite directions ($\Delta\theta = 180^\circ$) had the same probability of being connected and synapse strength as two neurons that prefer the same direction ($\Delta\theta = 0^\circ$). This can be contrasted with “direction-based” asymmetric rules, where neurons preferring opposite directions of motion are treated differently from ones preferring the same direction (Figure 6A). We reasoned that low levels of direction selectivity are due to the absence of such direction-based rules, because the symmetric rules enhance neurons’ responses to their anti-preferred direction due to inputs from oppositely tuned neurons. However, the models are also grounded in data, which show symmetric like-to-like rules for probability of E-to-E connections and no like-to-like rules for I-to-E connections (see above, although data are mostly limited to connection classes in L2/3). We assumed that all E-to-E connection probabilities obey the symmetric rule. Therefore, the only remaining flexibility is in the rules specifying synaptic weights.

Available data from L2/3 (Cossell et al., 2015; Znamenskiy et al., 2018) indicate that synaptic amplitude correlates with similarity of responses, for both E-to-E and I-to-E connected pairs. However, similarity of preferred direction alone is a poor predictor of synaptic strength for E-to-E connections, whereas similarity of receptive fields (ON-OFF overlap) is a better predictor (Cossell et al., 2015). Furthermore, *in vivo* patch-clamp measurements in L4 indicate that excitatory neurons responding to a drifting grating in phase with each other are preferentially connected (Lien and Scanziani, 2013). Motivated by these observations, we introduce two modifications to the synaptic strength rules: (1) a direction-of-motion-based like-to-like Gaussian profile for all connection classes (Figure 6A) and, (2) for the E-to-E classes only, a decrease of synaptic strength with distance in retinotopic visual space between source and target neurons, projected on the target neuron’s preferred direction (Figure 6B).

No other distance dependency in synaptic strength was introduced. Rule (2) confines the sources of strong connections to a stripe perpendicular to the target neuron’s preferred direction, biasing inputs to come primarily from neurons that respond in phase with the target neuron when stimulated by a drifting grating or edge (Figure 6B). These assumptions are consistent with optimal Bayesian synaptic connectivity (Iyer and Mihalas,

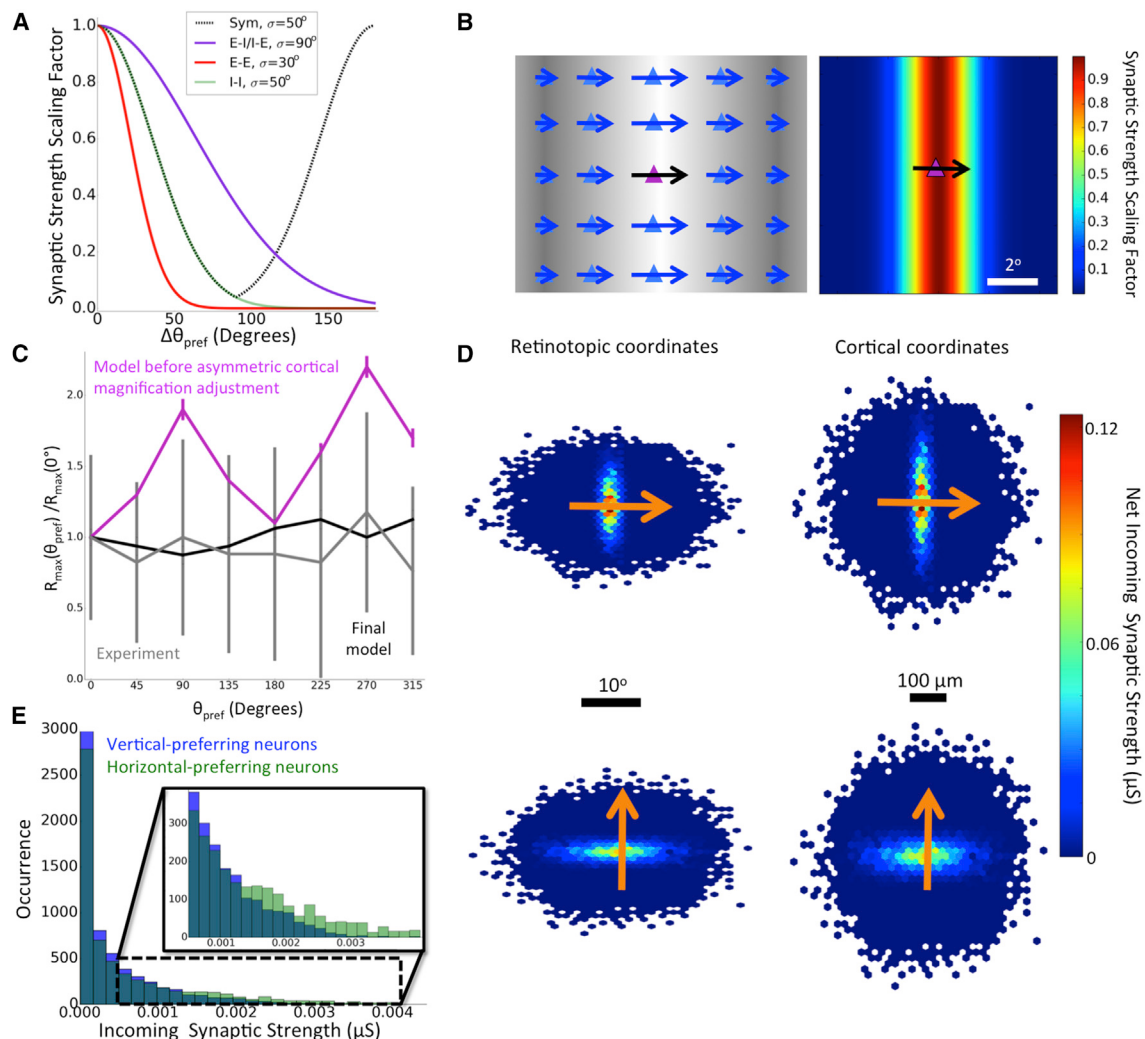


Figure 6. Refined Synaptic Functional Connections

(A) The original symmetric rule from the intermediate model (dotted black, “Sym”; Figure 4D) and the refined, asymmetric or “direction-based” (colors) synaptic strength profiles as a function of the difference between the preferred angles in two connected neurons. The like-to-like rule for E-to-E connection probabilities remains symmetric (Figure 4D), and no like-to-like rules are applied to other connection probabilities.

(B) The phase-based rule for synaptic strengths of E-to-E connections. Left: schematic of neurons preferring 0° direction is shown, as they respond to a 0° drifting grating (background shows phase alignment with the drifting grating). Arrow lengths are proportional to phase overlap with center (purple) neuron. Right: stronger weights are assigned to phase-matched neurons (heatmap illustrates the scaling factor applied in the models).

(C) Firing rates of excitatory neurons in response to their preferred drifting grating direction (median \pm SEM across trials) for the biophysical model. Applying the rules from (A) and (B) results in a firing rate bias for vertical- versus horizontal-preferring neurons due to differential cortical magnification (magenta); the bias is not observed experimentally (gray). The bias disappears when direction-dependent scaling is applied to synaptic weights according to the target neuron’s assigned preferred angle (black).

(D) Net synaptic inputs for horizontal- and vertical-preferring E4 biophysical neurons (rules in A and B and the additional direction-dependent scaling) in retinotopic (left) and cortical (right) coordinates (averages over 100 neurons after aligning their centers). The connection rules are also included here (distance dependence and symmetric like-to-like rules).

(E) Histogram of incoming synaptic weights onto E4 neurons based on their preferred direction. Horizontal-preferring neurons have a heavier tail than vertical-preferring neurons.

2017). We incorporated rules (1) and (2) at the synaptic strength level although the connection probabilities are governed by a distance-dependent rule and a symmetric like-to-like connectivity rule.

We tested 8 specific choices of rules (1) and (2), sampling multiple parameters for each (over 100 variants in total), primarily

employing the GLIF V1 model (Figure S4) before converging on a final set (Figure 6A). With a sufficiently narrow Gaussian curve characterizing the direction-based dependence on $\Delta\theta$ (Figure 6A), substantial improvement in DSI is obtained across all layers (Figure S5). This allows us to predict that like-to-like rules (1) and (2) above apply, potentially with cell-class-specific

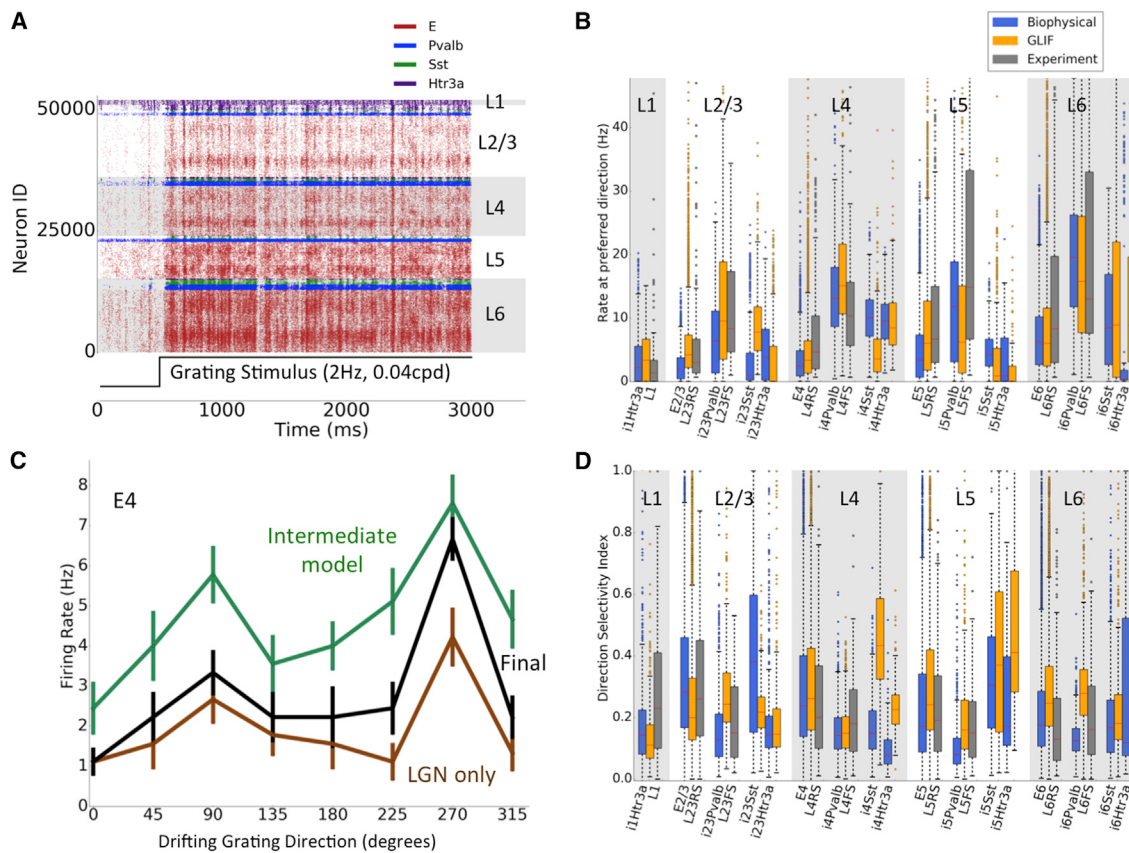


Figure 7. Simulated Responses to Drifting Gratings for the Final Cortical Recurrent Connectivity Rules (from Figure 6)

- (A) Raster plot in response to a drifting grating (note strong responses of the cells that prefer this grating's direction; neuron IDs are sorted within each class by the preferred angle).
- (B) Peak firing rates.
- (C) Example tuning curves (mean \pm SEM across 10 trials) for an E4 neuron from the final and intermediate (Figure 5C) models and no recurrent connections (Figure 3D).
- (D) DSI for the final V1 models and *in vivo* recordings.

parameters (Figure 6A). Given that different parameter values for rules (1) and (2) result in networks with robust levels of direction selectivity, the set (Figure 6A) we use for subsequent simulations is representative. In the absence of direct experimental measurements, we simply note that application of rules (1) and (2) with sufficiently narrow profiles enables amplification of direction selectivity by recurrent connections.

These rules, however, introduce a bias: vertical-preferring neurons exhibit higher peak firing rates than horizontal-preferring neurons; such a bias is *not* observed experimentally (Figure 6C). The root cause is the asymmetric retinotopic magnification in cortex (Schuett et al., 2002; Kalatsky and Stryker, 2003), which we implemented in our models (see STAR Methods). Specifically, moving along the horizontal direction in the cortical retinotopic map (azimuth) by 100 μ m corresponds to $\sim 7^\circ$ in the visual space, whereas along the vertical direction (elevation) 100 μ m corresponds to $\sim 4^\circ$. Consequently, the stripe from rule (2) (Figure 6B) is wider in cortical space for vertical- than for horizontal-preferring neurons, thus providing stronger net inputs from presynaptic V1 neurons (Figure S6). Because such a firing rate bias is not empirically observed

(Figure 6C), some mechanisms must adjust for the horizontal-vertical mismatch of translating retinotopy to connectivity. We implement one possible mechanism, the scaling of the strength of recurrent connections, where horizontal-preferring neurons receive synapses scaled by $0.5 \times (7 + 4)/4 = 1.38$ and vertical-preferring neurons scaled by $0.5 \times (7 + 4)/7 = 0.79$, with a linear interpolation in between (see STAR Methods). This approach fixes the firing rate bias (Figures 6C and S6).

In the final model, horizontal- and vertical-preferring cells receive, on average, equal excitatory synaptic input, sourced from the same size of stripes in retinotopic space but different widths in physical space (Figure 6D; the distance dependence contribution results in a finite stripe length). The resulting distribution of incoming weights predicts a heavier tail for horizontal- than for vertical-preferring neurons (Figure 6E).

With these finalized models, we simulated drifting gratings (Figures 7A and 7B; S scores for firing rate: E-biophysical = 0.80; E-GLIF = 0.89; Pvalb-biophysical = 0.85; Pvalb-GLIF = 0.88). Note the emergence of horizontal patches of elevated

firing (Figure 7A) due to pronounced direction selectivity not previously present (Figure 5A). For excitatory cells, the OSI distributions approximately match experimental recordings (Figure S6; S scores: E-biophysical = 0.87; E-GLIF = 0.89; Pvalb-biophysical = 0.47; Pvalb-GLIF = 0.78). Most importantly, the match of DSI to experimental values (Figures 7C and 7D; S scores: E-biophysical = 0.91; E-GLIF = 0.86; Pvalb-biophysical = 0.79; Pvalb-GLIF = 0.81) is improved (c.f. Figures 5C and 5D). Average tuning curves across models and experiments are shown in Figure S6. The Sst and Htr3a interneurons exhibit DSIs equal or higher than those of Pvalb interneurons, consistent with experiments (Kerlin et al., 2010; Ma et al., 2010). Thus, these new rules successfully enable direction selectivity in distinct populations of neurons while obeying diverse empirical constraints.

Both models maintain strong similarity with one another (S values: E-rates = 0.87; E-OSI = 0.85; E-DSI = 0.91; Table S1). We also calculated the pairwise similarity score between all the mice from our experiments and found median similarity scores (between animals) for firing rate, OSI, and DSI to be in the range [0.81, 0.84] for RS and [0.64, 0.66] for FS neurons, providing upper limits for matching experimental data given the inter-animal variability; as shown above, performance of our final models is close to these limits in most cases. Finally, our dynamics-based metrics still maintain a strong match with experiments (Figure S6).

We confirmed that, if like-to-like synaptic weight rules for E-to-Sst or Htr3a neurons are replaced with uniform synaptic weights, these neuron classes lose their orientation and direction selectivity (Figure S7), supporting our prediction that their orientation and direction tuning is due to local, recurrent connections. A sensitivity analysis with the GLIF network model (sweeping through the major synaptic strength parameters: E-to-E; E-to-I; I-to-E; and I-to-I) shows (Figure S7) that we found a suitable, though not unique, parameter regime. Not surprisingly, we observe tradeoffs across the sampled values of parameters, where improvement in one metric comes at the detriment of another.

Simulating the Models Using Diverse Stimuli

With this final model in place, we simulate responses to drastically different stimuli—flashes, natural movies, and a looming disk (Figure 8). For the flashes and natural movies stimuli, corresponding experimental data were available and compared against (Figure S8). This demonstrates the utility of our model to test any visual stimuli. Constructing a new stimulus is simply a matter of creating a monochromatic (x, y, t) movie (frames through time) and running it through our LGN filters via the BMTK code (see *Getting Started* in STAR Methods).

With full-field flashes, one of the strongest stimuli to test the stability of the network, our models remain stable and show strong onset and offset responses (Figures 8A–8C). The natural movie (Figure 8A) induces varied spatiotemporal patterns (Figure 8B) and a strong stimulus-onset response (Figure 8C). Experimental measurements to both flash and natural movies are publicly available from the Allen Brain Observatory (de Vries et al., 2020; Siegle et al., 2019); a thorough comparison with the models can be found in Figure S8.

As a further illustration, we simulated a looming disk (Figure 8A; see *STAR Methods*), a popular stimulus (e.g., Gabbiani et al., 2002; Yilmaz and Meister, 2013). Our network responds vigorously (Figure 8B), with differences in the time course of population firing rates between layers (Figure 8C). The population firing rate in L5 grows with the stimulus, although other layers show a transient response. The model predicts that different layers may exhibit different proportions of transient and ramping responses, which will be investigated in future experiments.

DISCUSSION

We here present two variants of a simulated mouse primary visual cortex. Both have an identical network graph, with ~230,000 nodes of two different flavors, either biophysically elaborate or highly simplified neurons. The variants were constrained by a plethora of experimental data: the morphologies of neurons and their firing behavior in response to somatic current injections; LGN filters; thalamocortical connectivity; recurrent connectivity; and activity patterns observed *in vivo*. This work continues the trend of developing increasingly more sophisticated models of cortical circuits in general (Traub et al., 2005; Zhu et al., 2009; Potjans and Diesmann, 2014; Markram et al., 2015; Arkhipov et al., 2018; Joglekar et al., 2018; Schmidt et al., 2018; Dura-Bernal et al., 2019) and visual cortex in particular (Wehmeier et al., 1989; Troyer et al., 1998; Zemel and Sejnowski, 1998; Krukowski and Miller, 2001; Arkhipov et al., 2018; Antolík et al., 2019). Our main goal was to integrate existing and emerging multi-modal datasets describing the structure and function of cortical circuits into biologically realistic network models.

Our models are represented with a standardized data format SONATA (Dai et al., 2020; <https://github.com/alleninstitute/sonata>) via the BMTK (<https://alleninstitute.github.io/bmtk/>; Gratiy et al., 2018). Simulations were carried out on 384 CPU cores for the biophysical and 1 core for GLIF network. The biophysical network requires ~90 min and the GLIF network ~4 min for 1 s of simulation, amounting to an almost four-orders-of-magnitude-greater computational cost for the former.

Although our models are similar in size and scope to the Blue Brain Project's network model of rat somatosensory cortex (Markram et al., 2015), they also differ in several ways, besides the distinction of visual versus somatosensory cortex. Prior to this publication, all components of our models and code are freely and publicly available (<https://portal.brain-map.org/explore/models/mv1-all-layers>) and can be replicated by any user with internet access (in particular the computationally less demanding GLIF model). Further, because we turned our efforts primarily toward comparing simulations with *in vivo* experiments, we supply biologically realistic visual stimuli to our models. Thus, we employed a large body of functional data constraining thalamo-cortical inputs and allowing arbitrary visual stimuli (movies) to be simulated. This contrasts with the somatosensory model that primarily simulated current injections into somas or spiking inputs from 10 thalamic fibers. In studying recurrent connectivity, we emphasized the functional logic of connection probabilities and synaptic strengths, which takes into account the stimulus tuning and the potential computational roles of neurons in the

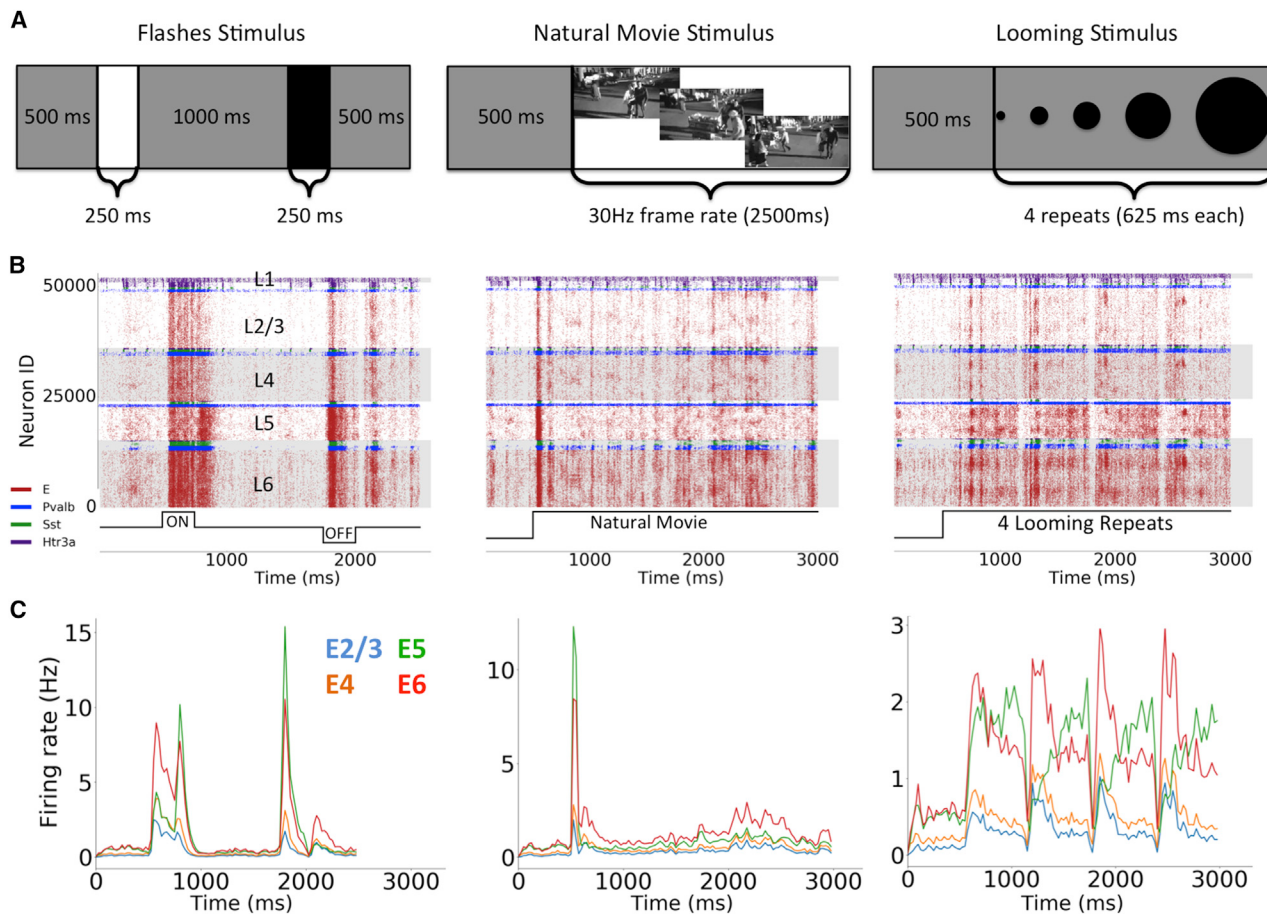


Figure 8. Responses of V1 Models to Diverse Stimuli

- (A) Responses of V1 models to full-field flashes, a natural movie, and a looming disk, all preceded by 500 ms of gray screen. Comparisons with experiments in Figure S8 are shown.
- (B) Example raster plots for all three stimuli.
- (C) Mean population firing rates for excitatory neurons.

circuit, besides the purely structural rules. As a result of these choices, we identified a number of experimentally testable predictions concerning the relations between the connectional properties and functional tuning of neurons.

Recent studies (Rössert et al., 2016; Amsalem et al., 2020; Arkhipov et al., 2018) demonstrated that the conversion of a biophysical network model to a GLIF counterpart can result in good qualitative and quantitative agreement in spiking output. We here likewise observed agreement between the biophysical and GLIF models. Although the connectivity graphs are identical, the input-output function of every neuron is different; yet, to judge by their firing rate distributions, the two models act similarly at the population level. This reveals, yet again, the perhaps unreasonable effectiveness of point neuron models given their vastly reduced degrees of freedom (Koch 1999). This is true for both passive (Arkhipov et al., 2018) and active dendritic models (Rössert et al., 2016). This system level effectiveness originates from effectiveness at the single-cell level: the individual GLIF (Teeter et al., 2018) and biophysical models (Gouwens et al., 2018) we use show similar levels of explained variance when

mapping a noisy current injection at the soma to an output spike train. It is possible that future models that reconstruct and simulate neurons using dendritic current measurements will outperform the network models presented here. Nevertheless, our results support applicability of the computationally less expensive GLIF network models (approximately >8,000 times faster), although ultimately, the level of resolution to use must be based on the scientific question under investigation. For instance, computing the extracellular field potential requires spatially extended neurons (Rall and Shepherd, 1968; Lindén et al., 2011; Einevoll et al., 2013; Reimann et al., 2013; Hagen et al., 2019). Developing our V1 simulacra at two levels of resolution enables a larger spectrum of possible studies.

In the process of building and testing the models, we made three major predictions about structure-function relationships in V1. The first addresses observations that non-Pvalb interneurons (Htr3a/VIP and Sst) show direction and orientation tuning (Liu et al., 2009; Kerlin et al., 2010; Ma et al., 2010) but receive connections from other V1 neurons that are distributed uniformly rather than a like-to-like fashion (Fino and Yuste, 2011) and receive little

to no LGN input (Ji et al., 2016). We thus implemented like-to-like rules for synaptic strengths of E-to-Sst or Htr3a connections, resulting in robust tuning of Htr3a and Sst classes (the tuning was lost when the rule was removed; Figure S7).

Our second prediction extends from experiments investigating functional connections between excitatory neurons (Bock et al., 2011; Ko et al., 2011; Cossell et al., 2015; Wertz et al., 2015; Lee et al., 2016), thus far primarily in L2/3. Our results suggest that synaptic weights follow rules that are different from the rules that connect two neurons in the first place: whereas the latter are organized in a like-to-like symmetric manner (Ko et al., 2011), the former follow asymmetric (direction-dependent) rules (Figure 6A). In our models, these weight rules were implemented among excitatory and inhibitory populations within and across layers (Figure 6A) to enable realistic levels of orientation and direction tuning (Figures 7C, 7D, and S6). How can this be reconciled with the report (Cossell et al., 2015) that similarity of preferred direction is not a good predictor of synaptic strength (in L2/3)? Because our models employ additional phase-dependent rules (Figures 6B and 6E), where incoming connection weights are close to zero outside of a stripe perpendicular to the target neuron's preferred direction, many presynaptic neurons that share the target neuron's direction preference connect very weakly to it (if outside the stripe). Therefore, direction similarity by itself is not a strong determinant of weights in our models either, whereas it does determine the weights if combined with the phase-related geometric constraints. Interestingly, as we were finalizing this report, a new experimental study (Rossi et al., 2019) appeared, showing (in L2/3) the preferential location of presynaptic neurons to be within a stripe, as in our connectivity implementation (Figures 6B and 6E), thus supporting our prediction (although the new data suggest this architecture may be realized in connection probabilities rather than in synaptic weights).

Our third prediction concerns the asymmetry in cortical retinotopic mapping between the horizontal and vertical axes (Schueft et al., 2002; Kalatsky and Stryker, 2003). This results in higher firing rates for vertical- than for horizontal-preferring neurons, which is not observed experimentally (Figure 6C). We thus infer the existence of one or more compensatory mechanisms, which may occur at many levels, including connection probability, LGN projections, etc. Our models addressed this at the synaptic strength level (Figures 6E and 6F).

These three predictions concern important relationships between the circuit structure and *in vivo* function. The first prediction is significant because mechanisms of tuning of Sst and Htr3a/VIP interneurons are likely to be critical in enabling diverse Sst- and Htr3a-mediated functions (e.g., Liu et al., 2009; Kerlin et al., 2010; Ma et al., 2010; Adesnik et al., 2012; Pfeffer et al., 2013; Fu et al., 2014; Tremblay et al., 2016; Muñoz et al., 2017). The second prediction suggests a set of general mechanisms that apply across cortical layers and neuronal classes to shape the computations of orientation and direction selectivity. The third prediction illuminates the potentially widespread wiring and/or homeostatic mechanisms that equalize firing rates between vertical- and horizontal-preferring neurons. All three predictions

are amenable to experimental tests (Bock et al., 2011; Hofer et al., 2011; Ko et al., 2011; Cossell et al., 2015; Wertz et al., 2015; Lee et al., 2016; Znamenskiy et al., 2018; Rossi et al., 2019).

Our models are freely accessible for download via the Allen Institute web portal at <https://portal.brain-map.org/explore/models/mv1-all-layers>. We hope that the community will exploit these resources to investigate more biologically refined models of cortex, the most complex piece of active matter in the known universe.

STAR★METHODS

Detailed methods are provided in the online version of this paper and include the following:

- LEAD CONTACT AND MATERIALS AVAILABILITY
- EXPERIMENTAL MODELS AND SUBJECT DETAILS
- METHOD DETAILS
 - Getting started
 - Instantiating the network
 - Forming Thalamocortical Connections
 - Background Connectivity
 - Recurrent Connectivity
 - Orientation Rule for Synaptic Strength
 - Electrophysiological Recordings
- QUANTIFICATION AND STATISTICAL ANALYSIS
 - Firing Rates
 - Orientation Selectivity Index (OSI)
 - Direction Selectivity Index (DSI)
 - Response at Preferred Direction
 - Signal Correlations, Noise Correlations, and Correlation of Signal and Noise Correlations
 - Lifetime and Population Sparsity
 - Similarity Score
- DATA AND CODE AVAILABILITY
- ADDITIONAL RESOURCES

SUPPLEMENTAL INFORMATION

Supplemental Information can be found online at <https://doi.org/10.1016/j.neuron.2020.01.040>.

ACKNOWLEDGMENTS

We thank Marius Pachitariu for providing spike-sorting code and assistance. We thank the Allen Institute founder, Paul G. Allen, for his vision, encouragement, and support.

AUTHOR CONTRIBUTIONS

Conceptualization, Y.N.B., C.K., and A.A.; Methodology, Y.N.B., B.C., R.I., N.W.G., K.D., S.L.G., S.M., and A.A.; Software, Y.N.B., B.C., K.D., S.L.G., and A.A.; Formal Analysis, Y.N.B., R.A.-A., and A.A.; Data Curation, Y.N.B., B.C., X.J., J.H.S., and S.R.O.; Writing – Original, Y.N.B. and A.A.; Writing – Review & Editing, Y.N.B., C.K., and A.A.; Visualization, Y.N.B., S.L.G., K.D., and A.A.; Supervision, S.M., C.K., and A.A.

DECLARATION OF INTERESTS

The authors declare no competing interests.

Received: June 25, 2019

Revised: October 17, 2019

Accepted: January 27, 2020

Published: March 3, 2020

REFERENCES

- Adesnik, H., Bruns, W., Taniguchi, H., Huang, Z.J., and Scanziani, M. (2012). A neural circuit for spatial summation in visual cortex. *Nature* **490**, 226–231.
- Amsalem, O., Eyal, G., Rogozinski, N., Gevaert, M., Kumbhar, P., Schürmann, F., and Segev, I. (2020). An efficient analytical reduction of detailed nonlinear neuron models. *Nat. Commun.* **11**, 288.
- Amunts, K., Ebner, C., Müller, J., Telefont, M., Knoll, A., and Lippert, T. (2016). The human brain project: creating a European research infrastructure to decode the human brain. *Neuron* **92**, 574–581.
- Antolík, J., Monier, C., Frégnac, Y., and Davison, A.P. (2019). A comprehensive data-driven model of cat primary visual cortex. *bioRxiv*. <https://doi.org/10.1101/416156>.
- Arenz, A., Drews, M.S., Richter, F.G., Ammer, G., and Borst, A. (2017). The temporal tuning of the *Drosophila* motion detectors is determined by the dynamics of their input elements. *Curr. Biol.* **27**, 929–944.
- Arkhipov, A., Gouwens, N.W., Billeh, Y.N., Gratiy, S., Iyer, R., Wei, Z., Xu, Z., Abbasi-Asl, R., Berg, J., Buice, M., et al. (2018). Visual physiology of the layer 4 cortical circuit in silico. *PLoS Comput. Biol.* **14**, e1006535.
- Beierlein, M., and Connors, B.W. (2002). Short-term dynamics of thalamocortical and intracortical synapses onto layer 6 neurons in neocortex. *J. Neurophysiol.* **88**, 1924–1932.
- Beierlein, M., Gibson, J.R., and Connors, B.W. (2003). Two dynamically distinct inhibitory networks in layer 4 of the neocortex. *J. Neurophysiol.* **90**, 2987–3000.
- Billeh, Y.N., Iyer, R., Wahle, I.A., Caldejón, S., Durand, S., Groblewski, P.A., Larkin, J.D., Lecoq, J., Williford, A., Mihalas, S., et al. (2019). Widespread presence of direction-reversing neurons in the mouse visual system. *bioRxiv*. <https://doi.org/10.1101/826701>.
- Bock, D.D., Lee, W.C., Kerlin, A.M., Andermann, M.L., Hood, G., Wetzel, A.W., Yurgenson, S., Soucy, E.R., Kim, H.S., and Reid, R.C. (2011). Network anatomy and in vivo physiology of visual cortical neurons. *Nature* **471**, 177–182.
- Bopp, R., Holler-Rickauer, S., Martin, K.A., and Schuhknecht, G.F. (2017). An ultrastructural study of the thalamic input to layer 4 of primary motor and primary somatosensory cortex in the mouse. *J. Neurosci.* **37**, 2435–2448.
- Borst, A., and Egelhaaf, M. (1989). Principles of visual motion detection. *Trends Neurosci.* **12**, 297–306.
- Bortone, D.S., Olsen, S.R., and Scanziani, M. (2014). Translaminar inhibitory cells recruited by layer 6 corticothalamic neurons suppress visual cortex. *Neuron* **82**, 474–485.
- Cauli, B., Audinat, E., Lambolez, B., Angulo, M.C., Ropert, N., Tsuzuki, K., Hestrin, S., and Rossier, J. (1997). Molecular and physiological diversity of cortical nonpyramidal cells. *J. Neurosci.* **17**, 3894–3906.
- Chevée, M., and Brown, S.P. (2018). The development of local circuits in the neocortex: recent lessons from the mouse visual cortex. *Curr. Opin. Neurobiol.* **53**, 103–109.
- Cossell, L., Iacaruso, M.F., Muir, D.R., Houlton, R., Sader, E.N., Ko, H., Hofer, S.B., and Mrsic-Flogel, T.D. (2015). Functional organization of excitatory synaptic strength in primary visual cortex. *Nature* **518**, 399–403.
- Dai, K., Hernando, J., Billeh, Y.N., Gratiy, S.L., Planas, J., Davison, A.P., Dura-Bernal, S., Gleeson, P., Devresse, A., Dichter, B.K., et al. (2020). The SONATA data format for efficient description of large-scale network models. *PLoS Comput. Biol.* **16**, e1007696.
- Dantzker, J.L., and Callaway, E.M. (2000). Laminar sources of synaptic input to cortical inhibitory interneurons and pyramidal neurons. *Nat. Neurosci.* **3**, 701–707.
- de Vries, S.E.J., Lecoq, J.A., Buice, M.A., Groblewski, P.A., Ocker, G.K., Oliver, M., Feng, D., Cain, N., Ledochowitsch, P., Millman, D., et al. (2020). A large-scale, standardized physiological survey reveals functional organization of the mouse visual cortex. *Nat. Neurosci.* **23**, 138–151.
- Douglas, R.J., and Martin, K.A. (2007). Recurrent neuronal circuits in the neocortex. *Curr. Biol.* **17**, R496–R500.
- Douglas, R.J., Martin, K.A.C., and Whitteridge, D. (1989). A canonical microcircuit for neocortex. *Neural Comput.* **1**, 480–488.
- Douglas, R.J., Koch, C., Mahowald, M., Martin, K.A., and Suarez, H.H. (1995). Recurrent excitation in neocortical circuits. *Science* **269**, 981–985.
- Dura-Bernal, S., Neymotin, S.A., Suter, B.A., Shepherd, G.M.G., and Lytton, W.W. (2019). Multiscale dynamics and information flow in a data-driven model of the primary motor cortex microcircuit. *bioRxiv*. <https://doi.org/10.1101/201707>.
- Durand, S., Iyer, R., Mizuseki, K., de Vries, S., Mihalas, S., and Reid, R.C. (2016). A comparison of visual response properties in the lateral geniculate nucleus and primary visual cortex of awake and anesthetized mice. *J. Neurosci.* **36**, 12144–12156.
- Egger, R., Schmitt, A.C., Wallace, D.J., Sakmann, B., Oberlaender, M., and Kerr, J.N. (2015). Robustness of sensory-evoked excitation is increased by inhibitory inputs to distal apical tuft dendrites. *Proc. Natl. Acad. Sci. USA* **112**, 14072–14077.
- Einevoll, G.T., Kayser, C., Logothetis, N.K., and Panzeri, S. (2013). Modelling and analysis of local field potentials for studying the function of cortical circuits. *Nat. Rev. Neurosci.* **14**, 770–785.
- Einevoll, G.T., Destexhe, A., Diesmann, M., Grün, S., Jirsa, V., de Kamps, M., Migliore, M., Ness, T.V., Plesser, H.E., and Schürmann, F. (2019). The scientific case for brain simulations. *Neuron* **102**, 735–744.
- Fino, E., and Yuste, R. (2011). Dense inhibitory connectivity in neocortex. *Neuron* **69**, 1188–1203.
- Fu, Y., Tucciarone, J.M., Espinosa, J.S., Sheng, N., Darcy, D.P., Nicoll, R.A., Huang, Z.J., and Stryker, M.P. (2014). A cortical circuit for gain control by behavioral state. *Cell* **156**, 1139–1152.
- Gabbiani, F., Krapp, H.G., Koch, C., and Laurent, G. (2002). Multiplicative computation in a visual neuron sensitive to looming. *Nature* **420**, 320–324.
- Gewaltig, M.-O., and Diesmann, M. (2007). Nest (neural simulation tool). *Scholarpedia* **2**, 1430.
- Gouwens, N.W., Berg, J., Feng, D., Sorensen, S.A., Zeng, H., Hawrylycz, M.J., Koch, C., and Arkhipov, A. (2018). Systematic generation of biophysically detailed models for diverse cortical neuron types. *Nat. Commun.* **9**, 710.
- Gouwens, N.W., Sorensen, S.A., Berg, J., Lee, C., Jarsky, T., Ting, J., Sunkin, S.M., Feng, D., Anastassiou, C.A., Barkan, E., et al. (2019). Classification of electrophysiological and morphological neuron types in the mouse visual cortex. *Nat. Neurosci.* **22**, 1182–1195.
- Gratiy, S.L., Billeh, Y.N., Dai, K., Mitelut, C., Feng, D., Gouwens, N.W., Cain, N., Koch, C., Anastassiou, C.A., and Arkhipov, A. (2018). BioNet: a Python interface to NEURON for modeling large-scale networks. *PLoS ONE* **13**, e0201630.
- Hagen, E., Næss, S., Ness, T.V., and Einevoll, G.T. (2019). LFPy – multimodal modeling of extracellular neuronal recordings in Python. *bioRxiv*. <https://doi.org/10.1101/620286>.
- Harris, K.D., and Mrsic-Flogel, T.D. (2013). Cortical connectivity and sensory coding. *Nature* **503**, 51–58.
- Harris, K.D., and Shepherd, G.M.G. (2015). The neocortical circuit: themes and variations. *Nat. Neurosci.* **18**, 170–181.
- Hines, M.L., and Carnevale, N.T. (1997). The NEURON simulation environment. *Neural Comput.* **9**, 1179–1209.
- Hofer, S.B., Ko, H., Pichler, B., Vogelstein, J., Ros, H., Zeng, H., Lein, E., Lesica, N.A., and Mrsic-Flogel, T.D. (2011). Differential connectivity and response dynamics of excitatory and inhibitory neurons in visual cortex. *Nat. Neurosci.* **14**, 1045–1052.
- Iyer, R., and Mihalas, S. (2017). Cortical circuits implement optimal context integration. *bioRxiv*. <https://doi.org/10.1101/158360>.

- Ji, X.Y., Zingg, B., Mesik, L., Xiao, Z., Zhang, L.I., and Tao, H.W. (2016). Thalamocortical innervation pattern in mouse auditory and visual cortex: laminar and cell-type specificity. *Cereb. Cortex* 26, 2612–2625.
- Jiang, X., Wang, G., Lee, A.J., Stornetta, R.L., and Zhu, J.J. (2013). The organization of two new cortical interneuronal circuits. *Nat. Neurosci.* 16, 210–218.
- Jiang, X., Shen, S., Cadwell, C.R., Berens, P., Sinz, F., Ecker, A.S., Patel, S., and Tolias, A.S. (2015). Principles of connectivity among morphologically defined cell types in adult neocortex. *Science* 350, aac9462.
- Joglekar, M.R., Mejias, J.F., Yang, G.R., and Wang, X.J. (2018). Inter-areal balanced amplification enhances signal propagation in a large-scale circuit model of the primate cortex. *Neuron* 98, 222–234.e8.
- Juavinett, A.L., Nauhaus, I., Garrett, M.E., Zhuang, J., and Callaway, E.M. (2017). Automated identification of mouse visual areas with intrinsic signal imaging. *Nat. Protoc.* 12, 32–43.
- Jun, J.J., Steinmetz, N.A., Siegle, J.H., Denman, D.J., Bauza, M., Barbarits, B., Lee, A.K., Anastassiou, C.A., Andrei, A., Aydin, Ç., et al. (2017). Fully integrated silicon probes for high-density recording of neural activity. *Nature* 551, 232–236.
- Kalatsky, V.A., and Stryker, M.P. (2003). New paradigm for optical imaging: temporally encoded maps of intrinsic signal. *Neuron* 38, 529–545.
- Kerlin, A.M., Andermann, M.L., Berezovskii, V.K., and Reid, R.C. (2010). Broadly tuned response properties of diverse inhibitory neuron subtypes in mouse visual cortex. *Neuron* 67, 858–871.
- Kloc, M., and Maffei, A. (2014). Target-specific properties of thalamocortical synapses onto layer 4 of mouse primary visual cortex. *J. Neurosci.* 34, 15455–15465.
- Ko, H., Hofer, S.B., Pichler, B., Buchanan, K.A., Sjöström, P.J., and Mrsic-Flogel, T.D. (2011). Functional specificity of local synaptic connections in neocortical networks. *Nature* 473, 87–91.
- Koch, C. (1999). *Biophysics of Computation: Information Processing in Single Neurons* (Oxford University Press).
- Koch, C., and Jones, A. (2016). Big science, team science, and open science for neuroscience. *Neuron* 92, 612–616.
- Krukowski, A.E., and Miller, K.D. (2001). Thalamocortical NMDA conductances and intracortical inhibition can explain cortical temporal tuning. *Nat. Neurosci.* 4, 424–430.
- Lee, S., Hjerling-Leffler, J., Zagha, E., Fishell, G., and Rudy, B. (2010). The largest group of superficial neocortical GABAergic interneurons expresses ionotropic serotonin receptors. *J. Neurosci.* 30, 16796–16808.
- Lee, W.-C.A., Bonin, V., Reed, M., Graham, B.J., Hood, G., Glattfelder, K., and Reid, R.C. (2016). Anatomy and function of an excitatory network in the visual cortex. *Nature* 532, 370–374.
- Lefort, S., Tomm, C., Floyd Sarria, J.C., and Petersen, C.C. (2009). The excitatory neuronal network of the C2 barrel column in mouse primary somatosensory cortex. *Neuron* 61, 301–316.
- Levy, R.B., and Reyes, A.D. (2012). Spatial profile of excitatory and inhibitory synaptic connectivity in mouse primary auditory cortex. *J. Neurosci.* 32, 5609–5619.
- Lien, A.D., and Scanziani, M. (2013). Tuned thalamic excitation is amplified by visual cortical circuits. *Nat. Neurosci.* 16, 1315–1323.
- Lien, A.D., and Scanziani, M. (2018). Cortical direction selectivity emerges at convergence of thalamic synapses. *Nature* 558, 80–86.
- Lindén, H., Tetzlaff, T., Potjans, T.C., Pettersen, K.H., Grün, S., Diesmann, M., and Einevoll, G.T. (2011). Modeling the spatial reach of the LFP. *Neuron* 72, 859–872.
- Liu, B.H., Li, P., Li, Y.T., Sun, Y.J., Yanagawa, Y., Obata, K., Zhang, L.I., and Tao, H.W. (2009). Visual receptive field structure of cortical inhibitory neurons revealed by two-photon imaging guided recording. *J. Neurosci.* 29, 10520–10532.
- Ma, W.P., Liu, B.H., Li, Y.T., Huang, Z.J., Zhang, L.I., and Tao, H.W. (2010). Visual representations by cortical somatostatin inhibitory neurons—selective but with weak and delayed responses. *J. Neurosci.* 30, 14371–14379.
- Markram, H., Muller, E., Ramaswamy, S., Reimann, M.W., Abdellah, M., Sanchez, C.A., Ailamaki, A., Alonso-Nanclares, L., Antille, N., Arsever, S., et al. (2015). Reconstruction and simulation of neocortical microcircuitry. *Cell* 163, 456–492.
- Martin, C.L., and Chun, M. (2016). The BRAIN initiative: building, strengthening, and sustaining. *Neuron* 92, 570–573.
- Mercer, A., West, D.C., Morris, O.T., Kirchhecker, S., Kerkhoff, J.E., and Thomson, A.M. (2005). Excitatory connections made by presynaptic cortico-cortical pyramidal cells in layer 6 of the neocortex. *Cereb. Cortex* 15, 1485–1496.
- Morgenstern, N.A., Bourg, J., and Petreanu, L. (2016). Multilaminar networks of cortical neurons integrate common inputs from sensory thalamus. *Nat. Neurosci.* 19, 1034–1040.
- Movshon, J.A., Thompson, I.D., and Tolhurst, D.J. (1978). Spatial summation in the receptive fields of simple cells in the cat's striate cortex. *J. Physiol.* 283, 53–77.
- Muñoz, W., Tremblay, R., Levenstein, D., and Rudy, B. (2017). Layer-specific modulation of neocortical dendritic inhibition during active wakefulness. *Science* 355, 954–959.
- Narayanan, R.T., Egger, R., Johnson, A.S., Mansvelder, H.D., Sakmann, B., de Kock, C.P., and Oberlaender, M. (2015). Beyond columnar organization: cell type- and target layer-specific principles of horizontal axon projection patterns in rat vibrissal cortex. *Cereb. Cortex* 25, 4450–4468.
- Nicola, W., and Clopath, C. (2017). Supervised learning in spiking neural networks with FORCE training. *Nat. Commun.* 8, 2208.
- Niell, C.M., and Stryker, M.P. (2008). Highly selective receptive fields in mouse visual cortex. *J. Neurosci.* 28, 7520–7536.
- Oh, S.W., Harris, J.A., Ng, L., Winslow, B., Cain, N., Mihalas, S., Wang, Q., Lau, C., Kuan, L., Henry, A.M., et al. (2014). A mesoscale connectome of the mouse brain. *Nature* 508, 207–214.
- Oláh, S., Füle, M., Komlósi, G., Varga, C., Báldi, R., Barzó, P., and Tamás, G. (2009). Regulation of cortical microcircuits by unitary GABA-mediated volume transmission. *Nature* 461, 1278–1281.
- Olsen, S.R., Bortone, D.S., Adesnik, H., and Scanziani, M. (2012). Gain control by layer six in cortical circuits of vision. *Nature* 483, 47–52.
- Packer, A.M., and Yuste, R. (2011). Dense, unspecific connectivity of neocortical parvalbumin-positive interneurons: a canonical microcircuit for inhibition? *J. Neurosci.* 31, 13260–13271.
- Pfeffer, C.K., Xue, M., He, M., Huang, Z.J., and Scanziani, M. (2013). Inhibition of inhibition in visual cortex: the logic of connections between molecularly distinct interneurons. *Nat. Neurosci.* 16, 1068–1076.
- Pillow, J.W., Paninski, L., Uzzell, V.J., Simoncelli, E.P., and Chichilnisky, E.J. (2005). Prediction and decoding of retinal ganglion cell responses with a probabilistic spiking model. *J. Neurosci.* 25, 11003–11013.
- Piscopo, D.M., El-Danaf, R.N., Huberman, A.D., and Niell, C.M. (2013). Diverse visual features encoded in mouse lateral geniculate nucleus. *J. Neurosci.* 33, 4642–4656.
- Potjans, T.C., and Diesmann, M. (2014). The cell-type specific cortical microcircuit: relating structure and activity in a full-scale spiking network model. *Cereb. Cortex* 24, 785–806.
- Rall, W., and Shepherd, G.M. (1968). Theoretical reconstruction of field potentials and dendrodendritic synaptic interactions in olfactory bulb. *J. Neurophysiol.* 31, 884–915.
- Reimann, M.W., Anastassiou, C.A., Perin, R., Hill, S.L., Markram, H., and Koch, C. (2013). A biophysically detailed model of neocortical local field potentials predicts the critical role of active membrane currents. *Neuron* 79, 375–390.
- Reimann, M.W., King, J.G., Muller, E.B., Ramaswamy, S., and Markram, H. (2015). An algorithm to predict the connectome of neural microcircuits. *Front. Comput. Neurosci.* 9, 120.
- Rössert, C., Pozzorini, C., Chindemi, G., Davison, A.P., Eroe, C., King, J., Newton, T.H., Nolte, M., Ramaswamy, S., Reimann, M.W., et al. (2016).

- Automated point-neuron simplification of data-driven microcircuit models. arXiv, arXiv:1604.00087v2 <https://arxiv.org/abs/1604.00087>.
- Rossi, L.F., Harris, K.D., and Carandini, M. (2019). Excitatory and inhibitory intracortical circuits for orientation and direction selectivity. bioRxiv. <https://doi.org/10.1101/556795>.
- Schaub, M.T., Billeh, Y.N., Anastassiou, C.A., Koch, C., and Barahona, M. (2015). Emergence of slow-switching assemblies in structured neuronal networks. *PLoS Comput. Biol.* 11, e1004196.
- Schmidt, M., Bakker, R., Hilgetag, C.C., Diesmann, M., and van Albada, S.J. (2018). Multi-scale account of the network structure of macaque visual cortex. *Brain Struct. Funct.* 223, 1409–1435.
- Schoonover, C.E., Tapia, J.C., Schilling, V.C., Wimmer, V., Blazeski, R., Zhang, W., Mason, C.A., and Bruno, R.M. (2014). Comparative strength and dendritic organization of thalamocortical and corticocortical synapses onto excitatory layer 4 neurons. *J. Neurosci.* 34, 6746–6758.
- Schuetz, S., Bonhoeffer, T., and Hübener, M. (2002). Mapping retinotopic structure in mouse visual cortex with optical imaging. *J. Neurosci.* 22, 6549–6559.
- Schüz, A., and Palm, G. (1989). Density of neurons and synapses in the cerebral cortex of the mouse. *J. Comp. Neurol.* 286, 442–455.
- Schwalger, T., and Chizhov, A.V. (2019). Mind the last spike - firing rate models for mesoscopic populations of spiking neurons. *Curr. Opin. Neurobiol.* 58, 155–166.
- Seabrook, T.A., Burbridge, T.J., Crair, M.C., and Huberman, A.D. (2017). Architecture, function, and assembly of the mouse visual system. *Annu. Rev. Neurosci.* 40, 499–538.
- Seeman, S.C., Campagnola, L., Davoudian, P.A., Hoggarth, A., Hage, T.A., Bosma-Moody, A., Baker, C.A., Lee, J.H., Mihalas, S., et al. (2018). Sparse recurrent excitatory connectivity in the microcircuit of the adult mouse and human cortex. *eLife* 7, e37349.
- Siegle, J.H., López, A.C., Patel, Y.A., Abramov, K., Ohayon, S., and Voigts, J. (2017). Open Ephys: an open-source, plugin-based platform for multichannel electrophysiology. *J. Neural Eng.* 14, 045003.
- Siegle, J.H., Jia, X., Durand, S., Gale, S., Bennett, C., Graddis, N., Heller, G., Ramirez, T.K., Choi, H., Luviano, J.A., et al. (2019). A survey of spiking activity reveals a functional hierarchy of mouse corticothalamic visual areas. bioRxiv. <https://doi.org/10.1101/805010>.
- Song, S., Sjöström, P.J., Reigl, M., Nelson, S., and Chklovskii, D.B. (2005). Highly nonrandom features of synaptic connectivity in local cortical circuits. *PLoS Biol.* 3, e68.
- Sussillo, D., and Abbott, L.F. (2009). Generating coherent patterns of activity from chaotic neural networks. *Neuron* 63, 544–557.
- Szabadics, J., Tamás, G., and Soltesz, I. (2007). Different transmitter transients underlie presynaptic cell type specificity of GABA_A, slow and GABA_A, fast. *Proc. Natl. Acad. Sci. USA* 104, 14831–14836.
- Tasic, B., Yao, Z., Graybuck, L.T., Smith, K.A., Nguyen, T.N., Bertagnolli, D., Goldy, J., Garren, E., Economo, M.N., Viswanathan, S., et al. (2018). Shared and distinct transcriptomic cell types across neocortical areas. *Nature* 563, 72–78.
- Teeter, C., Iyer, R., Menon, V., Gouwens, N., Feng, D., Berg, J., Szafer, A., Cain, N., Zeng, H., Hawrylycz, M., et al. (2018). Generalized leaky integrate-and-fire models classify multiple neuron types. *Nat. Commun.* 9, 709.
- Teeters, J.L., Godfrey, K., Young, R., Dang, C., Friedsam, C., Wark, B., Asari, H., Peron, S., Li, N., Peyrache, A., et al. (2015). Neurodata without borders: creating a common data format for neurophysiology. *Neuron* 88, 629–634.
- Thomson, A.M., and Lamy, C. (2007). Functional maps of neocortical local circuitry. *Front. Neurosci.* 1, 19–42.
- Thomson, A.M., West, D.C., Wang, Y., and Bannister, A.P. (2002). Synaptic connections and small circuits involving excitatory and inhibitory neurons in layers 2–5 of adult rat and cat neocortex: triple intracellular recordings and biocytin labelling *in vitro*. *Cereb. Cortex* 12, 936–953.
- Traub, R.D., Contreras, D., Cunningham, M.O., Murray, H., LeBeau, F.E., Roopun, A., Bibbig, A., Wilent, W.B., Higley, M.J., and Whittington, M.A. (2005). Single-column thalamocortical network model exhibiting gamma oscillations, sleep spindles, and epileptogenic bursts. *J. Neurophysiol.* 93, 2194–2232.
- Tremblay, R., Lee, S., and Rudy, B. (2016). GABAergic interneurons in the neocortex: from cellular properties to circuits. *Neuron* 91, 260–292.
- Troyer, T.W., Kruckowski, A.E., Priebe, N.J., and Miller, K.D. (1998). Contrast-invariant orientation tuning in cat visual cortex: thalamocortical input tuning and correlation-based intracortical connectivity. *J. Neurosci.* 18, 5908–5927.
- van Santen, J.P.H., and Sperling, G. (1984). Temporal covariance model of human motion perception. *J. Opt. Soc. Am. A* 1, 451–473.
- Vélez-Fort, M., Rousseau, C.V., Niedworok, C.J., Wickersham, I.R., Rancz, E.A., Brown, A.P., Strom, M., and Margrie, T.W. (2014). The stimulus selectivity and connectivity of layer six principal cells reveals cortical microcircuits underlying visual processing. *Neuron* 83, 1431–1443.
- Vinje, W.E., and Gallant, J.L. (2000). Sparse coding and decorrelation in primary visual cortex during natural vision. *Science* 287, 1273–1276.
- Wehmeier, U., Dong, D., Koch, C., and Van Essen, D. (1989). Modeling the mammalian visual system. In *Methods in Neuronal Modeling: From Synapses to Networks*, C. Koch, I. Segev, T.J. Sejnowski, and T.A. Poggio, eds. (MIT Press), pp. 335–359.
- Wertz, A., Trenholm, S., Yonehara, K., Hillier, D., Raics, Z., Leinweber, M., Szalay, G., Ghanem, A., Keller, G., Rózsa, B., et al. (2015). Presynaptic networks. Single-cell-initiated monosynaptic tracing reveals layer-specific cortical network modules. *Science* 349, 70–74.
- West, D.C., Mercer, A., Kirchhecker, S., Morris, O.T., and Thomson, A.M. (2006). Layer 6 cortico-thalamic pyramidal cells preferentially innervate interneurons and generate facilitating EPSPs. *Cereb. Cortex* 16, 200–211.
- Yamins, D.L.K., and DiCarlo, J.J. (2016). Using goal-driven deep learning models to understand sensory cortex. *Nat. Neurosci.* 19, 356–365.
- Yilmaz, M., and Meister, M. (2013). Rapid innate defensive responses of mice to looming visual stimuli. *Curr. Biol.* 23, 2011–2015.
- Yoshimura, Y., Dantzker, J.L.M., and Callaway, E.M. (2005). Excitatory cortical neurons form fine-scale functional networks. *Nature* 433, 868–873.
- Zemel, R.S., and Sejnowski, T.J. (1998). A model for encoding multiple object motions and self-motion in area MST of primate visual cortex. *J. Neurosci.* 18, 531–547.
- Zhu, W., Shelley, M., and Shapley, R. (2009). A neuronal network model of primary visual cortex explains spatial frequency selectivity. *J. Comput. Neurosci.* 26, 271–287.
- Znamenskiy, P., Kim, M.-H., Muir, D.R., Iacaruso, M.F., Hofer, S.B., and Mrsic-Flogel, T.D. (2018). Functional selectivity and specific connectivity of inhibitory neurons in primary visual cortex. bioRxiv. <https://doi.org/10.1101/294835>.

STAR★METHODS

LEAD CONTACT AND MATERIALS AVAILABILITY

Further information and requests for resources should be directed to and will be fulfilled by the Lead Contact, Anton Arkhipov (antonat@alleninstitute.org). This study did not generate new unique reagents. The datasets and code generated are publicly available (see [Data and Code Availability](#)).

EXPERIMENTAL MODELS AND SUBJECT DETAILS

The *in vivo* extracellular recordings used for comparison with simulations are freely available: <https://portal.brain-map.org/explore/circuits/visual-coding-neuropixels> (Siegle et al., 2019).

METHOD DETAILS

Getting started

This section is a primer on how to start using our V1 network models employing the Brain Modeling ToolKit (BMTK; <https://alleninstitute.github.io/bmtk/> (Gratiy et al., 2018)). A thorough description can be found in the README file. The README file at the time of publication can be found in Supplemental Material 1.

The models of visual cortex have been run and tested with BMTK under Python 2.7 and 3.6. Note that since the models are provided as files in SONATA format (<https://github.com/AllenInstitute/sonata>, (Dai et al., 2020)), they can be simulated using other software besides BMTK, as long as this software supports SONATA.

Installation and tutorials

The first step is to learn how to use BMTK. The up-to-date instructions on using BMTK can be accessed at: <https://alleninstitute.github.io/bmtk/>.

Installation

The installation page on the website above describes how BMTK can be installed using a command line terminal. Installing BMTK will automatically install all the underlying Python packages dependencies. Users will need to install NEURON for the biophysical-level of granularity and NEST for the GLIF-level of granularity of the network models:

<https://www.neuron.yale.edu/neuron/download>
<https://nest-simulator.readthedocs.io/en/latest/installation/>

Users also have the option of using a Docker Image to build and simulate networks without needing to install the BMTK prerequisites on your computer (please see the BMTK website's Installation page for this particular approach).

Installing with pip

pip install bmtk

Installing from source

```
git clone https://github.com/AllenInstitute/bmtk
cd bmtk
python setup.py install
```

Installing using Anaconda

```
conda install -c kaeldai bmtk
```

Tutorials

The tutorials page on the BMTK website links to different chapters that guide users on how to build and simulate networks at both biophysical and GLIF levels of detail described in this manuscript. They start with single cell examples before moving to network examples. The landing page (Chapter 0) can be found here: https://github.com/AllenInstitute/bmtk/blob/develop/docs/tutorial_00_introduction.ipynb

The Primary Visual Cortex models

The portal for the models of primary visual cortex (V1) can be accessed at: <https://portal.brain-map.org/explore/models/mv1-all-layers>

All details of our release are described in the README file. Here we provide an introduction for running the model, analyzing outputs, creating arbitrary movies, and descriptions of the file format.

Metadata resources

The meta-data, curation of experimental data that was used to constrain and build our models are available freely under the metadata resources section as downloadable files. These include files that describe the V1 model structure (Figure 1), the number of synapses estimated (see below), the connection probabilities and connection strengths (Figure 4).

Running the models

Both models are run with BMTK using very similar commands. One simply needs to navigate to the correct directory (Biophysical or GLIF) and run the following commands:

1. Biophysical V1 network model (note for most biophysical simulations reported in this work, we used N = 384 parallel processes)

```
mpirun -np N nrniv -mpi -python run_bionet.py config.json
```

2. GLIF V1 network model (this runs on a single CPU)

```
python run_pointnet.py config.json
```

Note both commands call a config.json file in their respective directories. This file determines the configuration to be used for a simulation. In this file, users can set the duration of a simulation, the incoming spike trains, the connectivity, and many other simulation relevant conditions. The files are in the SONATA format. A thorough description of the format can be found in the SONATA paper (Dai et al., 2020) and at the SONATA GitHub page: <https://github.com/AllenInstitute/sonata>.

Simulation output and analysis

The complete simulation outputs from both models can be found in the output directories. The model portal repository provides scripts for creating raster plots such as those shown in Figures 3, 5, 7, and 8, as well as the code used for calculating other metrics reported in this work. For example, to create a raster plot, a user can simply run the following command:

```
python plot_raster.py
```

Creating arbitrary movies to present to the model

One of the main features of our model is the ability of users to simulate the response of visual cortex to arbitrary visual stimuli by showing any mono-chromatic movie (x, y, t) to the LGN filters to generate an appropriate spike train, simulating the output of four distinct classes of geniculate relay cells, that are then fed into the V1 models. We have provided pre-built examples for drifting grating stimuli and looming stimuli that can be found here:

<https://github.com/AllenInstitute/bmtk/tree/develop/docs/examples>

There is also a filter_movie directory (as an example) with 80 LGN units that can be exposed to any movie. A user can create and save any numpy file that is 3-dimensional (frames over time). The config.json file can be set to point to the saved file of interest and the output from the LGN can then be simulated.

For full integration with the LGN model used in this study, users can examine the drifting gratings class created in the python script movie.py in the LGN section of the release (lines 150 – 214).

Model components

The format of our network files are described extensively in our papers and resources we released (Gratiy et al., 2018; Dai et al., 2020, <https://github.com/AllenInstitute/sonata>). We briefly mention some of these components here.

Neurons

All relevant information about neurons is saved in two files, nodes.h5 and node_types.csv. The first file contains all unique information about neurons (e.g., location coordinates) while the second contains repeated information across neurons (e.g., layer information).

Connections

The connections, synaptic weights, and other connectivity-relevant parameters are stored in two files, edges.h5 and edge_types.csv. Similar to the nodes, the first file contains every unique connection while the second contains shared information between connections.

Simulation configuration

All simulation parameters and components needed to run a simulation are stored in a config.json file. This is the best starting point as it will contain pointers to all the relevant directories and files being used by a simulation.

Instantiating the network

The V1 neurons were instantiated and distributed through every layer with raw number estimates available in the supplemental document (document V1_structure.xlsx from our web portal available at <https://portal.brain-map.org/explore/models/mv1-all-layers>). We considered the estimated cell densities measured in every layer based on nuclear stains (Schüz and Palm, 1989) with the assumption of an 85% and 15% fractions for excitatory and inhibitory neurons, respectively. The fractions used for the interneuron classes were based on expression levels in double *in situ* hybridization experiments (Lee et al., 2010). The layer thicknesses were taken from the Allen Mouse Brain Atlas (see Cortical Layer Thickness Measurements). Our model incorporated inhibitory neurons in layers L2/3 through to L6 from three broad classes, Parvalbumin- (Pvalb), Somatostatin- (Sst), and Htr3a-positive; and excitatory neurons in each layer were considered as one class (Figures 1A and 1C). Layer 1 (L1) had only a single inhibitory class of Htr3a neurons (Lee et al., 2010; Tremblay et al., 2016). L2/3 excitatory neurons (class E2/3) were reconstructed from the Cux2 Cre-line, which is almost pan-excitatory in this layer. L4 excitatory cells were reconstructed from four populations

of cells studied in our slice recording pipeline (Gouwens et al., 2019) – the Scnn1a, Nr5a1, and Rorb Cre-lines, as well as reconstructions from non-Cre-animals. L5 excitatory neurons were sourced from two populations – the cells labeled by the Rbp4 Cre-line and unlabeled L5 neurons. Although L4 and L5 excitatory cells were reconstructed from multiple Cre-lines, it is not known whether cells labeled by these different Cre lines differ in connectivity. Furthermore, they do not appear to show substantially distinct patterns of activity *in vivo* under passive conditions (de Vries et al., 2020). Therefore, for all simulations and analyses we combined the L4 and L5 excitatory cells into a single class per layer (E4 and E5). L6 contained one excitatory class (E6), with neurons from Ntsr1 Cre-line only (due to availability at the time of creating the models). Altogether, we used 112 unique neuron models for the biophysical and 111 for the GLIF networks. At time of model building, there were no Htr3a reconstructions for L6 neurons and therefore we re-used the two deepest L5 Htr3a models to populate this cell class in L6. Although the Allen Cell Types Database had more cell models, not all models could fit geometrically in the V1 volume without protruding beyond the pia. This was due to Cre-lines not labeling specific layers exclusively, resulting in cases where cells from certain Cre-lines resided in adjacent layers (see [Somatic Coordinates](#)).

The neuron models were fit to *in-vitro* measurements (Gouwens et al., 2018; Teeter et al., 2018) and are publicly available via the Allen Cell Types Database (<http://celltypes.brain-map.org/>). All our biophysical models used passive dendrites although the Allen Cell Types Database includes neuron models with active dendritic conductances. This was due to active-dendritic models being too computationally expensive (prohibitively) for the extent of our work. Further, the somatic spike output from the active-dendrite models do not show much better performance than the models with active conductances restricted to the soma (<http://celltypes.brain-map.org/>). Therefore, we used the less computationally expensive neuron models.

Cortical Layer Thickness Measurements

Layer thicknesses for the model were taken from the Allen Mouse Brain Atlas (Oh et al., 2014 – <http://atlas.brain-map.org/>). They were calculated from a mouse common coordinate framework in which voxels were annotated with cortical areas and layers. In this framework, streamlines were calculated that connected pia to white matter using the shortest paths (Oh et al., 2014 - Documentation in <http://atlas.brain-map.org/>). For each voxel on the surface of V1, the thickness of each layer was calculated along the associated streamline, and the median values across all of V1 were used to construct the model.

Somatic Coordinates

With the number of neurons identified (V1_structure.xlsx), we needed to assign somatic coordinates for every cell and select appropriate neuron models. For the biophysically detailed neurons we also had to assign to a neuron a rotation about the depth axis (white-matter to pia). This is due to our V1 model using a fixed number of reconstructed neuron models relative to the total number of neurons simulated and hence when reusing a model, we randomly rotated the individual neurons between 0 and 2π around the depth axis. For the somatic coordinates, cells for each population were uniformly distributed within a cylindrical domain and within the specified layer depth. For the biophysical models, the depth of a neuron would affect which neuron model was assigned to it. The first condition was that a model would not be assigned to a particular cell if that model's morphology significantly extended out of the pia when placed at the cell's somatic location (with a tolerance of 100 μm). Once all putative cell models that pass this criterion were identified, we randomly selected a model based on a Gaussian probability density function (with standard deviation of 20 μm).

Visual Coordinates

Neurons' positions are defined in the physical space, whereas visual stimuli (see [Visual Stimuli](#)) supplied to the models, as well as the LGN filters converting these stimuli to spike trains impinging on V1 neurons, are defined in the visual space. Thus, a mapping between the two spaces needs to be defined. The cortical plane (plane perpendicular to the depth axis) was mapped to the visual space, with the geometrical center of the model corresponding to the center of the visual space. Retinotopic mapping experiments in the mouse V1 identified how much displacement in visual cortex corresponded to displacements in visual space (Schuett et al., 2002; Kalatsky and Stryker, 2003). Using these results (Figure 3 from Schuett et al., 2002 and Figure 4 from Kalatsky and Stryker, 2003), we approximated that the visual degrees traversed per mm of cortex are 70 degrees/mm in the azimuth and 40 degrees/mm in elevation. Note the asymmetry between the two directions. From this we can convert any translation of azimuth and elevation in cortex to a translation in visual space. For example, consider moving 845 μm in the azimuth (radius of the V1 model): the movement in visual space is then estimated to be $0.845 \text{ mm} * 70 \text{ degrees/mm} = 59.15 \text{ degrees}$. The somatic position of every neuron was used, via such translations, to establish the assigned neuron's position in the visual space, which was then used in algorithms establishing connectivity from the LGN to V1 (see below).

Distributing LGN Units

We sought to create an LGN model that roughly captures the entire LGN with an estimated 18,000 neurons in the mouse. In our model, we do not explicitly model the shell and core of the LGN and simply distribute the LGN units on a 2D plane in visual space to model 240 degrees (horizontal) by 120 degrees (vertical). We imposed a lattice structure on the 2D plane by dividing it into girds (15 blocks horizontally by 10 blocks vertically of size 16x12 degrees). Each block had a total of 116 LGN units ([Table 1](#)) distributed uniformly within the block to give a total of 17,400 LGN units that can process arbitrary visual stimuli.

Table 1. Distribution of LGN Unit Numbers in Every Block and the Receptive Field Sizes per Class

LGN Class	Units per Block	Spatial Size Range (Degrees)
sON-TF1	7	[2, 9]
sON-TF2	5	[2, 9]
sON-TF4	7	[2, 9]
sON-TF8	15	[2, 9]
sOFF-TF1	8	[2, 9]
sOFF-TF2	8	[2, 9]
sOFF-TF4	15	[2, 9]
sOFF-TF8	8	[2, 9]
sOFF-TF15	7	[2, 9]
tOFF-TF4	10	[2, 9]
tOFF-TF8	5	[2, 9]
tOFF-TF15	8	[2, 9]
sONsOFF	8	6
sONtOFF	5	9

Each LGN unit is represented by a spatio-temporally separable filter, which operated on the movies in the visual space as inputs, and returned a time series of the instantaneous firing rate as output (this rate was then converted to spikes in each individual trial using a Poisson process). The spatial components of the LGN filters are spatially symmetric two-dimensional Gaussian kernels and the temporal components are a sum of weighted raised-cosine bump basis functions (Pillow et al., 2005). The temporal kernel was designed to have a bi-phasic impulse response:

$$D_t^F(\tau) = w_1 b(\tau; t_1, d_1) + w_2 b(\tau; t_2, d_2),$$

$$b(\tau; t, d) = \frac{\cos(\log(t + \tau) - d) + 1}{2}$$

where there are six parameters: i) two time constants (t_1, t_2) for the basis functions, ii) two weights (w_1, w_2) used to linearly sum the functions and iii) offsets (d_2, d_1). All data and code are available through the BMTK (<https://alleninstitute.github.io/bmtk>). The spatial and temporal filters are combined to form a 3D spatiotemporal kernel to respond to input signals that are grayscale, represented on a –1 to 1 scale (from black to white), with a time step of 1 ms.

The LGN filters were sampled from 14 classes (Table 1) that approximated the diversity observed in experimental recordings *in vivo* (Durand et al., 2016) (see Main Text and Figure 2A). The LGN filter parameters used for every class were obtained by fitting filter responses to the mean experimental responses for every class (resulting parameter values are available in the BMTK). A $\pm 2.5\%$ jitter was added for every parameter when instantiating individual LGN filters. We observed that receptive field sizes of cells from most of the LGN classes in the experimental recordings (Durand et al., 2016) spanned a large range within class. We thus assigned every LGN unit a randomly generated spatial size within the recorded ranges drawn from a triangular distribution defined as follows: zero at lower bound, peak at the lower bound plus 1 degree, and then zero again at the upper bound (to approximate the experimental distributions).

Thalamocortical Architecture Impact on Direction Selectivity

The major guiding purpose for creating thalamocortical connections in our V1 models was to enable direction selectivity, which was proposed to arise due to integration of sustained and transient LGN inputs by V1 cells (Lien and Scanziani, 2018). Before instantiating such rules for the full-scale model, we performed a simplified theoretical analysis to investigate how combinations of transient and sustained pools of LGN inputs, using biologically realistic parameters, would create direction-selective responses in target V1 cells. For this analysis we approximated the LGN input to a V1 cell using a sustained ON and a transient OFF subfields.

For the thalamocortical projections to a V1 neuron in our full models (see Forming Thalamocortical Connections), we would first identify all suitable LGN filters that have overlapping retinotopic positions with the V1 cell. This pool of filters was then split into a sustained subfield ellipse in one half of the receptive field and a transient subfield ellipse in the other half (Figure 2C). The orientation of the ellipses would depend on the assigned preferred angle of the V1 neuron. The ellipses' major axis would be perpendicular to the preferred direction of the V1 neuron and the sustained subfield would be positioned such that it is activated first in the case of a bar moving in the preferred direction of the V1 neuron (Figure 2D). We would then randomly select filters from within these ellipses from the population of sustained or transient LGN filters (Figures 2C and 3A). For the simplified theoretical analysis here, we consider the sustained ON and transient OFF subfields, represented by a single elliptical filter each, approximating contributions from all LGN cells within a subfield.

The synaptic input current from one of the subfields (labeled as $F = \text{ON}$ or $F = \text{OFF}$) to the V1 cell in response to a stimulus is then described by

$$I^F(t) = \Gamma \text{ReLU}\left(r_{sp}^F + L^F(t)\right), \quad (1)$$

where Γ is the constant determining the magnitude of the current (assumed to be the same for both subfields), r_{sp}^F is a baseline (spontaneous) firing rate, and $\text{ReLU}(x)$ is a rectified linear unit function that is zero below a threshold (here set at zero) and linear above the threshold. The response is dependent on the stimulus $S(x,y,t)$:

$$L^F(t) = \int_0^\infty d\tau \int dx dy R^F(x,y,\tau) S(x,y,t-\tau), \quad (2)$$

We consider the case where the two subfields are offset along the x axis, so that each subfield is described as:

$$R^F(x,y,t) = D_s(x - l^F, y) D_t^F(t). \quad (3)$$

The assumption used here is that each kernel is spatio-temporally separable.

The temporal kernel used here is a sum of weighted raised-cosine bump basis functions as used above (Pillow et al., 2005; see [Distributing LGN units](#)). The spatial kernel is described by an elliptical Gaussian profile:

$$D_s(x,y) = \frac{1}{2\pi\sigma_x\sigma_y} \exp\left(-\frac{x^2}{2\sigma_x^2} - \frac{y^2}{2\sigma_y^2}\right). \quad (4)$$

with the standard deviations σ_x, σ_y , respectively. We will study a special case of subfields separated by a distance d along the x axis using $I^{ON} = d/2$ and $I^{OFF} = -d/2$:

$$\begin{aligned} R^{ON}(x,y,t) &= D_s\left(x - \frac{d}{2}, y\right) D_t^{ON}(t), \\ R^{OFF}(x,y,t) &= D_s\left(x + \frac{d}{2}, y\right) D_t^{OFF}(t) \end{aligned} \quad (5)$$

Let us examine the response of a cell to moving grating stimuli having maximum luminance S_{max} and a contrast c :

$$S(x,y,t) = \frac{1}{2} S_{max} (1 + c \cos(k_x x + k_y y - \omega t)) \quad (6)$$

where $\mathbf{k} = (k_x, k_y)$ defines the direction of the grating wave front: $k_x = k \cos(\theta)$, $k = 2\pi SF$, $\omega = 2\pi TF$ and SF (cpd) and TF (Hz) are the spatial and temporal frequencies of a grating, respectively.

It is more convenient to work in the complex space:

$$S(x,y,t) = \frac{1}{2} S_{max} + \frac{1}{2} c S_{max} \text{Re}\left\{e^{-i(k_x x + k_y y - \omega(t-\tau))}\right\} \quad (7)$$

The input current from each subfield is $I^F = \Gamma \text{ReLU}(r_{sp}^F + L^F(t))$ where r_{sp}^F is independent of stimulus and $L^F(t) = L_0^F + L_1^F$ is a stimulus dependent response:

$$L_1^F(t) = S_1 \text{Re} \left\{ \int_0^\infty d\tau \int dx dy R^F(x,y,\tau) e^{-i(k_x x + k_y y - \omega(t-\tau))} \right\} \quad (8)$$

$$L_0^F = S_0 \int_0^\infty d\tau \int dx dy R^F(x,y,\tau) \quad (9)$$

Here we use a short hand notation $S_1 = (1/2)cS_{max}$ and $S_0 = (1/2)S_{max}$.

Substituting $R^F(x,y,t)$ we find:

$$L_1^F(t) = S_1 \text{Re} \left\{ e^{i\omega t} \int_0^\infty d\tau e^{-i\omega\tau} D_t^F(\tau) \int dx dy e^{-i(k_x x + k_y y)} D_s(x - l^F, y) \right\} \quad (10)$$

Since the temporal kernel $D_t^F(\tau) = 0$ when $\tau < 0$, we can simply extend the integration to negative infinity over τ .

The temporal integral in $L_1^F(t)$ is the Fourier transforms over time:

$$D_t^F(\omega) = \int_{-\infty}^{\infty} d\tau e^{-i\omega\tau} D_t^F(\tau) \quad (11)$$

that could be expressed using the magnitude $|D_t^F(\omega)|$ and phase $\psi^F(\omega)$:

$$D_t^F(\omega) = |D_t^F(\omega)| \exp(i\psi^F(\omega)) \quad (12)$$

The spatial integral in $L_1^F(t)$ is the spatial Fourier transform:

$$D_s^F(k_x, k_y, l^F) = \int dx dy e^{-i(k_x x + k_y y)} D_s(x - l^F, y) \quad (13)$$

Thus, we can express $L_1^F(t)$ as

$$L_1^F(t) = S_1 \operatorname{Re}\{e^{i\omega t} D_t^F(\omega) D_s^F(k_x, k_y, l^F)\} \quad (14)$$

Thus, the response to a drifting grating with temporal angular frequency ω is determined by the Fourier component at that frequency only. We can compute the temporal components (raised cosine bumps) Fourier transforms numerically.

We can compute the spatial transform analytically to find:

$$D_s^F(k_x, k_y, l^F) = \exp(-ik_x l^F) \exp\left(-\left(k_x^2 \sigma_x^2 + k_y^2 \sigma_y^2\right)/2\right) \quad (15)$$

which has an amplitude:

$$|D_s^F(k_x, k_y)| = \exp\left(-\left(k_x^2 \sigma_x^2 + k_y^2 \sigma_y^2\right)/2\right). \quad (16)$$

so that:

$$L_1^F(t) = S_1 |D_s^F(k_x, k_y)| \operatorname{Re}\left\{e^{i\omega t} |D_t^F(\omega)| e^{i\left(-\frac{k_x l^F}{2} + \psi^F(\omega)\right)}\right\} \quad (17)$$

The total input current to a cell is the sum from the two subfields:

$$I(t) = \Gamma(\operatorname{ReLU}(r_0^{ON} + L^{ON}(t)) + \operatorname{ReLU}(r_0^{OFF} + L^{OFF}(t))) \quad (18)$$

Using these equations, we can estimate both the direction selectivity index (DSI) and the orientation selectivity index (OSI) of the F0 and F1 components for a variety of filter parameters: subfield separation d , ellipse aspect ratio or width (determined by σ_x , σ_y), and temporal parameters. The F0 response is a commonly used metric that calculates the cycle average mean of the response to a drifting grating while the F1 component computes the modulation response at the input temporal frequency (Movshon et al., 1978).

We used filter parameters from sON-TF8 and tOFF-TF8 as well all other default values: $d = 5$ degrees (Lien and Scanziani, 2013), SF = 0.025cpd, TF = 8Hz, ellipse aspect ratio = 3.0, ellipse minor axis = 4.0 degrees. For a set of fixed stimulus (drifting grating), we changed one parameter at a time and observed the impact on OSI and DSI. For the distance between the elliptical sustained and transient subfields (d ; Figure S1A), we note that the F1 component switches direction preference (i.e., its DSI changes sign) as d grows, due to a shifting phase difference between the subfields. The DSI of the F0 component is always zero as the net input remains constant for the preferred and null directions, consistent with experimental recordings (Lien and Scanziani, 2013, 2018). On the other hand, the OSI of the F0 component is constant but non-zero due to the elliptical structure of the subfields that biases the net input per grating cycle for specific orientations (but not directions). The OSI of the F1 component is positive even when $d = 0$ due to the elliptical shape of the subfields (and temporal properties). Second, by varying the sustained time-to-peak parameter (starting from the transient subfield's time-to-peak of 30ms, Figure S1A), we observe, as expected, that asymmetry in the temporal properties of the subfields is essential for producing direction selectivity. There is no direction selectivity in the F1 component when both filters are identical temporally; but as the time-to-peak of the sustained subfield increases, there is a quick rise in F1 DSI. This is followed by a reversal in the direction preference for very high (non-biological) time-to-peak values. The F1 OSI shows a sharp monotonic decrease with the sustained time-to-peak while the F0 OSI is non-monotonic but roughly constant. Other changes investigated in the subfield parameters were the aspect ratio of the ellipses and the size of the ellipses that both showed relatively constant F1 DSI as both ellipse sizes were altered together (Figure S1A). On the other hand, the OSI values showed a monotonic increase with both illustrating the contribution of the elongated structure for endowing orientation selectivity. An aspect ratio of one still showed some orientation selectivity due to the temporal offsets of the filters giving slight orientation selectivity (our OSI metric is based on circular variance, see Orientation Selective Index below).

We next investigate the effect of changing the spatial frequency of the drifting grating (Figure S1B). As before, the F0 DSI always remains zero. As the spatial frequency increases, we again observe a reversal in the preferred direction for the F1 component as observed experimentally in mouse cortex (Billeh et al., 2019). For orientation selectivity, the F1 OSI shows a sigmoidal

increase as spatial frequency increased while the F0 OSI shows a peak with a fast decay due to reduced responsiveness of the LGN ellipses to high spatial frequencies. On the other hand, the F1 OSI is relatively flat while the F0 OSI shows a peak response as a function of temporal frequency, albeit with a slower decay, again due to the reduced responsiveness of the LGN subfields to high temporal frequencies (Figure S1B). For our choice of subfield parameters, the F1 DSI does not switch sign as we varied temporal frequency, but such switching can occur as observed experimentally and with different filter properties and time constants (Billeh et al., 2019).

In summary, these simplified calculations confirm that the overarching model of the integration of sustained and transient LGN responses (Lien and Scanziani, 2018) indeed enables directionally selective input currents into V1 cells when biologically realistic parameters are used. Given this reassuring result, the next step was to create a similar architecture of connections to the V1 model from the thousands of filters representing LGN cells in the visual space.

Forming Thalamocortical Connections

The connections from the LGN to V1 neurons followed an approach similar to previous work (Arkhipov et al., 2018). The first step was to establish shared retinotopy between the V1 neurons and the LGN units. The coordinates of the LGN units were in visual space (degrees) while the V1 neurons' coordinates were in regular 3D space mapped to the cortical surface and white-matter-to-pia depth (see [Somatic Coordinates](#)). By imposing that the center of the V1 model mapped to the center of the visual space, the location of each V1 neuron was converted to visual space using the cortical magnification factor, as described in section [Visual Coordinates](#). This procedure assigned each V1 neuron a position in visual space, which may be expected to correspond approximately to the center of that neuron's RF in the complete model. We then identified which LGN units would project to every V1 neuron (from the classes to receive LGN inputs; see Main Text and [Table 2](#)), as follows.

Table 2. Properties of the Subfields in the Visual Space Used to Select LGN Neurons Projecting to V1 Neurons (for Every Cell Class Receiving LGN Inputs; the Remaining Classes Are Assumed to Receive no LGN Input)

V1 Neuron Class	Connection Probability	Mean LGN Current (pA)	V1 TF (Hz)	S _{ON} Ratio	Separation Range (degs)	Width Range (degs)	Aspect Ratio Range	Number of Synapses
<i>i1Htr</i>	0.588	29.0	2.0	0.75	[6, 10]	[8.5, 11]	[2.2, 2.4]	10
<i>E2/3</i>	0.789	20.3	1.5	0.90	[4, 6]	[7.5, 9.5]	[3.4, 3.6]	15
<i>i2/3Pvalb</i>	0.824	50.8	2.0	0.75	[6, 10]	[10, 13]	[1.6, 1.8]	15
<i>E4</i>	1.000	46.0	2.0	0.90	[4, 6]	[7.5, 9.5]	[3.4, 3.6]	80
<i>i4Pvalb</i>	1.000	119.8	2.0	0.75	[6, 10]	[10, 13]	[1.6, 1.8]	75
<i>E5</i>	1.000	20.3	1.5	0.50	[8, 12]	[12, 16]	[1.6, 1.8]	15
<i>i5Pvalb</i>	1.000	63.7	2.0	0.50	[6, 10]	[10, 13]	[1.6, 1.8]	20
<i>E6</i>	0.778	17.1	1.5	0.90	[3, 4]	[9, 11]	[3.4, 3.6]	15
<i>i6Pvalb</i>	0.818	44.1	2.0	0.75	[6, 10]	[10, 13]	[1.6, 1.8]	10

The connection probability refers to probability a neuron receives input from the LGN (Ji et al., 2016). The mean LGN input current corresponds to the mean excitatory LGN current the neuron class receives (Lien and Scanziani, 2013; Ji et al., 2016) when voltage clamped at the inhibitory synapse reversal potential (see [Thalamocortical Synaptic Weights](#)). The V1 TF column represents the preferred temporal frequency of the V1 neuron class (Niell and Stryker, 2008; Durand et al., 2016). The S_{ON} ratio refers to the probability the sustained component will be ON instead of OFF (Lien and Scanziani, 2013)—the transient component was always OFF. The separation range refers to the distance between the sustained and transient subfield ellipses—E4 estimated from Lien and Scanziani (2013). The width range refers to the minor-axis width of the ellipses (diameter). The aspect ratio refers to the length of the major axis relative to the minor axis. Note the aspect ratio is relative to neurons' visual space center, and once sizes of LGN receptive fields are incorporated, the results match experimental measures (Lien and Scanziani, 2013) more accurately, as shown previously (Arkhipov et al., 2018). The final column refers to the number of synapses an LGN neuron makes to a V1 neuron if a connection exists. This was extrapolated from experimental work (Morgenstern, Bourg and Petreanu, 2016), as discussed in [Thalamocortical Synapse Estimate](#).

Given the directionally selective architecture to be imposed, every V1 neuron was assigned a preferred angle of stimulus motion to determine the placement of the elliptical subfields from which LGN units would be sampled (Figures 2C, 2D, and 3A). There was always a transient OFF subfield and a sustained subfield that was either ON or OFF (this choice was made based on the relative abundance of the different classes of LGN cells in our experimental recordings (Durand et al., 2016), as summarized in Figure 2A). The two subfields were identically oriented and offset by certain distance; the offset and the short axes of both ellipses were co-aligned with the assigned preferred direction of the target V1 neuron. The position of the target neuron was at the middle of the line connecting the centers of the two subfields (Figure 3A). The subfields were positioned along the vector of the preferred direction of the target neuron in such a way that the vector pointed from the sustained subfield to the transient one (Figures 2C and 2D). Note that the assigned angle was also used for the recurrent connectivity (see below) and was set such that every V1 neuron class represented every angle in the range [0, 360°] with even spacing. The dimensions of the subfields and their separation varied

based on the V1 neuron's class (Table 2); these choices were made according to estimates of the expected metrics – such as the OSIs and DSIs – for the class, based on experimental reports (see details and references in V1_parameter_estimate.pptx). The subfield parameters for the E4 target population were informed by our previous model of L4 (Arkhipov et al., 2018), and parameters for the other populations were chosen following the assumption that V1 cell classes with stronger orientation/direction selectivity would utilize smaller and more elongated LGN subfields. Importantly, we chose these subfield parameters once and did not vary them to tune the model for target OSI/DSI values. The good agreement with the experiment observed for the final model (Figure 7) suggests that our initial choice of these subfield parameters was appropriate (and, to the best of our knowledge, it is consistent with available experimental observations); however, it is possible that the agreement could be further improved by tuning the subfield parameters.

As reported previously, a linear angle approximation was used (Arkhipov et al., 2018). Further, every V1 neuron was assigned a preferred temporal frequency drawn from a Poisson distribution with a mean as measured experimentally (Table 2, (Niell and Stryker, 2008; Durand et al., 2016)). This determined the probability of selecting LGN units preferring particular temporal frequencies. Given that there was a discrete number of LGN filters for every class (sON, sOFF, tOFF), the probability of selecting a particular subclass (i.e., a particular TF) was based on the distance of the V1 neuron's temporal frequency from the LGN unit's preferred temporal frequency, divided by the total possible distance for that class.

Once the subfields were established, the LGN units to be connected to the target cell were selected among the units that had the centers of their spatial kernels within the subfields (and of the LGN class matching to each subfield, see Figure 3A). From this total pool, LGN units were connected randomly based on the probability of connections (given their temporal frequency as mentioned above). Thus, not every LGN unit in the subfield formed a connection with the target V1 cell (Figures 2C and 3A). Finally, for the ON/OFF filters, a restriction was set that required the axis of the ON/OFF subfield to be within 15-degrees relative to the assigned direction preference angle of the V1 neuron (Arkhipov et al., 2018). With all these choices, the suitable LGN units were selected probabilistically to project to each target V1 cell. Based on these rules, the average number of LGN units connecting to a V1 cell for excitatory neurons is: 19.3 ± 6.0 (mean \pm SD), median = 19, min = 2, max = 47. For inhibitory neurons: 15.0 ± 4.4 (mean \pm SD), median = 15, min = 2, max = 32. The mean number of LGN projecting units to V1 neurons is below the recently reported estimates (Lien and Scanziani, 2018); although the authors themselves acknowledge their measurements are likely overestimates. Nevertheless, the most important parameter is the total synaptic current that every population receives (see Thalamocortical Synaptic Weights) which was matched to experimental measurements (Lien and Scanziani, 2013, 2018) and could compensate for the differences we have in this version of the model.

Thalamocortical Synapse Estimate

For the biophysical model we estimated the number of synapses impinging on different V1 neurons. The exact numbers of synapses are only estimates as the more critical step was ensuring the total excitatory current received from the LGN matched experimental measurements (see below). Should the number of synapses be incorrectly estimated, this was compensated for by the final synaptic weights.

Our calculation and formalism for the number of thalamocortical synapses per neuron is described below; we also provide a supplementary document (Num_TC_synapses.xlsx) where all the calculations were done. As the field advances, in particular with electron-microscopy technology, we would need fewer assumptions and simply use the available data. In the model, synapses were placed along the dendrites up to 150 μm away from the soma but excluding the soma, as done in a previous model of the layer 4 of V1 based on experimental reports (Schoonover et al., 2014; Arkhipov et al., 2018)

One key resource we used was the fluorescence measurements of the density of thalamocortical axons across cortical depth (Morgenstern et al., 2016). We used this work to determine the fraction of fluorescence across cortical layers as an estimate of the fraction of LGN projections to different layers. The full calculation is in the accompanying supplemental document (Num_TC_synapses.xlsx) and here we explain our technique and assumptions. In particular we assume the Fluorescence Signal (FS) is a function of the following factors:

- 1) Number of cells in a layer (Schüz and Palm, 1989)
- 2) Percentage of cells that actually get innervated in a layer from the LGN (Ji et al., 2016)
- 3) At a specific depth (layer), the proportion of dendrites from cells in different layers that extend to other layers
 - a. For inhibitory neurons, dendrites where assumed to stay within their layers and not extend to other layers.
- 4) The fraction of LGN synapses on a stretch of dendrite is the same whether that dendrite is from an E or Pvalb cell.
 - a. Assumption includes that, out of all interneurons, Pvalb cells are the only ones to receive significant innervation except for layer 1 (Ji et al., 2016).

From here, for a specific layer, the below calculation was used to approximate the fluorescence signal (FS) from labeled thalamocortical axons. This example is for layer 4:

$$FS_{L4} = A * \left\{ N_{E4} * IR_{E4} * NTC_{E4} * Frac_{E4}^{L4} + \right. \\ \left. N_{i4Pvalb} * IR_{i4Pvalb} * NTC_{i4Pvalb} * Frac_{i4Pvalb}^{L4} + \right. \\ \left. N_{E5} * IR_{E5} * NTC_{E5} * Frac_{E5}^{L4} + \right. \\ \left. N_{E2/3} * IR_{E2/3} * NTC_{E2/3} * Frac_{E2/3}^{L4} \right\}$$

In the accompanying document, this is found by summing the rows for the gray matrix. The different notations mean:

- FS_{L4} = Fluorescence signal in layer 4
- A = Constant factor converting fluorescence signal to biological innervation numbers. We assume fluorescence is a linear function of axon density, and so A is constant for every layer. We will need to solve for A (see below)
- N_{E4} = Number of excitatory cells in L4 (Schüz and Palm, 1989)
- IR_{E4} = Innervation ratio of LGN onto L4 pyramids (Ji et al., 2016)
- NTC_{E4} = Number of synapses that are thalamocortical for every L4 excitatory cell – the numbers we are seeking for every layer. From (4) above, it is assumed that $NTC_{i4Pvalb} = NTC_{E4}$.
- $Frac_{E4}^{L4}$ = The fraction of excitatory cells' dendrites in L4 that is contributed from L4 cells (from assumption (3) above). See the light green matrix in the accompanying excel sheet.
- Note that $Frac_{E4}^{L4} + Frac_{E2/3}^{L4} + Frac_{E5}^{L4} = 1$.
- Note that we assumed $Frac_{E6}^{L4} = 0$ and thus that is not included in the above example of L4.
- Note that $Frac_{i4Pvalb}^{L4} = 1$ is assumed for all layers for Pvalbs (assumption (3.a) above).

We note that the document had a finer division of every layer (split in two: upper (A) and lower (B) components) and the idea of single layers here is just used for explanatory purposes.

All these assumptions can be written in a matrix form as follows:

$$FS = M_p \times NTC$$

Where FS is an Nx1 matrix of the fluorescence signal across layers and NTC is the Number of thalamocortical synapses that is also Nx1. M_p holds the properties described above and is a matrix of dimensions NxN (contributions from all layers). We can thus solve for NTC by taking the inverse:

$$NTC = M_p^{-1} \times FS$$

Since the constant factor A is not known, the values of NTC are not the actual numbers of synapses. To account for this, we use the experimental finding that, in the mouse visual cortex, the number of thalamocortical synapses on L4 excitatory cells is approximately 1200-1500 (Schoonover et al., 2014; Arkhipov et al., 2018). This gives us the scaling factor to account for A and hence allows us to estimate NTC for all layers.

For the supplemental document, which was divided into finer divisions, 1200 was used as the average of all the L4 divisions (see scaling factor). The final numbers of synapses are shown in Table 2.

Thalamocortical Synaptic Weights

Various studies have identified the thalamic innervation pattern into the visual cortex across laminae (Lien and Scanziani, 2013, 2018; Kloc and Maffei, 2014; Schoonover et al., 2014; Ji et al., 2016; Morgenstern et al., 2016; Bopp et al., 2017). We used these results to identify the total current that different cell classes should receive from the LGN. One study, already published during building of the model, measured that the net current into layer 4 excitatory cells responding to drifting gratings at their preferred angle was on average 46 pA (Lien and Scanziani, 2013). Other work using optogenetic stimulation identified the cell classes that are innervated by the thalamus, for both the probabilities and relative strengths (Ji et al., 2016). Assuming linear scaling to layer 4 excitatory neurons, we estimated the target mean current for every cell class in response to a grating at a neuron's preferred direction (Table 2).

To attain the target currents, for the biophysically detailed model, we created networks that had 100 cells from every model, all preferring a single direction, that receive LGN innervation as described above (but no other connections). A grating at 2Hz, full contrast, full field with a spatial frequency of 0.04 cycles per degree (to match the experimental work precisely (Lien and Scanziani, 2013)) was shown to these networks. Further, the neurons were clamped at the reversal potential of the inhibitory (GABA) synapses in our model (again as performed experimentally). The net mean current during exposure was measured and the synaptic weights iteratively adjusted until the target current was reached with 2% tolerance. For surrounding LIF neurons, for the same stimulus, we matched the firing rates that were observed with purely LGN input in the biophysically detailed core neurons of the same class. As mentioned in the Main Text, during optimization of the full V1 model the weights of synapses from LGN to excitatory layer 4 cells were not adjusted at all, given that the measurements we used as targets in the procedure described here were of high precision and obtained *in vivo* (which is the condition we were aiming to match in our full model). Weights of all other synapses from LGN were adjusted, but the adjustment was allowed to be no more than by a factor of 2 for the mean input current (Table 2).

Finally, the GLIF V1 model used the same strategy to attain the same target mean currents using the same grating LGN stimulus. However, as the GLIF models employed in the V1 model were using post-synaptic current based synapses (see **Synaptic Characteristics**), the weights were initially set as the target currents and no voltage clamping was required. However, the average rheobase (minimal current step amplitude to elicit an action potential) of the GLIF models in the model are bigger than experimental measurements, except for Pvalb neurons that had smaller rheobase values. To match closely to the experimental data, the established weights from LGN to V1 were scaled by the average ratio between average rheobase of GLIF model and experiment data i.e., 0.81 for Pvalb population and 1.36 for other populations.

Background Connectivity

A second source of input to the V1 models was a background to coarsely represent the “rest of the brain.” This was modeled as a single input unit that fired at 1 kHz with a Poisson distribution. All neurons received connections from this unit, and the weights were optimized (at the same time with the optimization of weights for the recurrent connectivity) to ensure the V1 spontaneous firing rates matched target experimental rates (see below).

Recurrent Connectivity

The cortico-cortical connection probabilities for different cell-class pairs were estimated based on an extensive and systematic survey of the existing literature and curated into a resource that we make publicly available (Figure 4, see details and notes regarding assumptions and the literature used in Connection_probabilities.pptx). It is important to note that in many cases the values reported in the literature do not take into account two effects that strongly influence connection probabilities. The first is distance dependence: cells closer to each other typically have a higher chance of being connected than cells further apart. The second is that connection probabilities can be affected strongly by differences or similarities in functional preferences of cells, such as preference for direction. Pyramidal cells in L2/3 of mouse V1, for instance, have a higher chance of being connected with one another if they prefer similar directions, compared to orthogonally tuned cells (Ko et al., 2011; Cossell et al., 2015; Wertz et al., 2015; Lee et al., 2016). Based on these two factors, the adjustments described below were made.

It is reasonable to assume, for the mouse visual cortex, that both these factors are independent (given the “salt and pepper” arrangement of orientation tuned cells in the mouse (Harris and Mrsic-Flogel, 2013; Seabrook et al., 2017)) and thus the total probability of connection for a cell-class pair is a product of the distance-dependent and preferred-angle-dependent factors (functions of r and $\Delta\phi$, respectively):

$$P_{src \rightarrow trg} = P_{dist}(r) \times P_{angle}(\Delta\phi)$$

First we will discuss each of the components separately, and the final section will illustrate our approach for combining the two.

Distance dependent adjustment

We noted that the majority of the experimental literature reporting probability of connections tended to consider inter-somatic distances that were within approximately 0 – 50 μm to 0 – 100 μm . Since we aimed to have a Gaussian profile for distance dependence (Levy and Reyes, 2012), the probability at the origin had to be adjusted to account for these measurements. Since measurements were made in the approximate range of 50 – 100 μm for the upper bound, we chose to consider the mid-point of 75 μm as our reference point for such upper bound. Note the distance is only measured in a plane and is independent of cortical depth in our calculations.

For the Gaussian probability distribution:

$$P_{dist}(r) = Ae^{-\frac{r^2}{\sigma^2}}$$

Given our assumptions, the integral of this probability from 0 to $R_0 = 75 \mu\text{m}$, divided by the area within the radius R_0 , should be equal to the reported measured probability, P_{rep} :

$$\frac{1}{\pi R_0^2} \int_0^{R_0} Ae^{-\frac{r^2}{\sigma^2}} dx dy = P_{rep}$$

Converting to polar coordinates:

$$\frac{1}{\pi R_0^2} \int_0^{R_0} Ae^{-\frac{r^2}{\sigma^2}} 2\pi r dr = P_{rep}$$

$$\frac{2A}{R_0^2} \int_0^{R_0} re^{-\frac{r^2}{\sigma^2}} dr = P_{rep}$$

$$-A \frac{\sigma^2}{R_0^2} \left[e^{-\frac{r^2}{\sigma^2}} \right]_{r=0}^{r=R_0} = P_{rep}$$

$$A \frac{\sigma^2}{R_0^2} \left(1 - e^{-\frac{R_0^2}{\sigma^2}} \right) = P_{rep}$$

$$A = \frac{P_{rep}}{\frac{\sigma^2}{R_0^2} \left(1 - e^{-\frac{R_0^2}{\sigma^2}} \right)}$$

This establishes the relationship between the values reported in the literature and our distance-dependent formula for connection probability.

From work in the mouse cortex (Levy and Reyes, 2012), the standard deviations were estimated to be (Figure 4):

$$\sigma_{E \rightarrow E} = 114 \mu m$$

$$\sigma_{E \rightarrow Pvalb} = 92 \mu m$$

$$\sigma_{E \rightarrow Sst} = 103 \mu m$$

$$\sigma_{Pvalb \rightarrow E} = 95 \mu m$$

$$\sigma_{Sst \rightarrow E} = 85 \mu m$$

From internal data at the Allen Institute during model building:

$$\sigma_{Pvalb \rightarrow Pvalb} \approx 120 \mu m$$

In the absence of data for other connection classes, we assumed that connections between excitatory neurons and Htr3a neurons follow the same dependence as between excitatory and Sst neurons (bidirectionally). Finally, we also assumed that connections among all inhibitory classes have the same distance dependence (i.e., same as $\sigma_{Pvalb \rightarrow Pvalb}$).

Direction tuning adjustment for excitatory-to-excitatory connections

For direction tuning dependence, our system is modeled such that pairs containing cells with similar preferred direction angles have higher connection probabilities than pairs of orthogonally tuned cells, when the presynaptic neuron is excitatory (like-to-like connectivity) (Ko et al., 2011; Cossell et al., 2015; Wertz et al., 2015; Lee et al., 2016). Here we assume the dependence is linear (Figure 4D) as a function of the direction tuning difference ($\Delta\phi$):

$$P_{angle}(\Delta\phi) = B_1 + G\Delta\phi$$

Since we considered direction selective tuning for connectivity (not direction selective), the difference of preferred angles of any two cells can be compressed to be between 0° and 90° . For this model, we can see that the intercept occurs at $(0^\circ, B_1)$. At the other extreme of the model, we set the point to be $(90^\circ, B_2)$. The relative strength of the dependence can be described by a ratio $Q = B_2/B_1$. As can be seen, for like-to-like, $Q < 1$ (i.e., $G < 0$).

Our model is developed such that the integral of the function $P_{angle}(\Delta\phi)$, normalized by the range of $\Delta\phi$, is always equal to 1. This was implemented because this function is used as a multiplier with the distance dependence function $P_{dist}(r)$, and since we assume that experimentalists measuring *in-vitro* probability of connections sample equally from cells preferring all possible direction angles *in vivo*. This does restrict the ratio Q one can select, based on the distance dependence and measured connection probabilities from experimental literature. As will be discussed below, if the ratio is outside of a suitable range, we rescaled it to reach the correct range.

Because $B_2 = QB_1$,

the gradient can be expressed as:

$$G = \frac{QB_1 - B_1}{90^\circ - 0^\circ} = \frac{B_1(Q - 1)}{90^\circ}$$

Integral of $P_{src \rightarrow trg}(\Delta\phi)$ (with normalization for the angle range) should be set to 1 to determine the scaling factor:

$$\frac{1}{90^\circ} \int_{0^\circ}^{90^\circ} (B_1 + G\Delta\phi) d\Delta\phi = 1$$

$$\frac{1}{90^\circ} \left[B_1 \Delta\phi + \frac{1}{2} G (\Delta\phi)^2 \right]_{0^\circ}^{90^\circ} = 1$$

$$B_1 + 45^\circ G = 1$$

Substitute G:

$$B_1 + 45^\circ \left(\frac{B_1(Q - 1)}{90^\circ} \right) = 1$$

Solving for B_1 :

$$B_1 = \frac{2}{1+Q}$$

And thus:

$$B_2 = \frac{2Q}{1+Q}$$

The value of Q for layers 2/3, 4, and 6 was set to 0.5 given the high direction selectivity (Niell and Stryker, 2008; Durand et al., 2016). For layer 5, it was set at 0.8 for the excitatory-to-excitatory connections due to lower direction selectivity in this layer (Niell and Stryker, 2008; Durand et al., 2016).

Combining distance-dependent and direction-dependent adjustments

As can be observed from the above, the scaling can increase the measured connection probability and to ensure our probabilities were never greater than 1, we forced the following condition:

$$A \times B_1 \leq 1$$

Thus, we used the following algorithm:

```
{
Calculate A
If A > 1,
Set A = 1.0
Calculate B1
If A * B1 > 1
Set B1_new = 1/A
Set B2 = B2 + (B1 - B1_new)
Set B1 = B1_new
Calculate G = (B2 - B1)/90°
# Intercept and gradient are determined and hence can apply P_angle(Δφ) formula.
}
```

In this formalism (pseudo-code above), if one selects a specific value of Q that happens to push the probability values above 1, the worst-case scenario would be that Q is rescaled to 1.0 and hence there is no direction tuning dependence. The trend will never reverse. And this scenario will only occur if there already exists a very high connectivity probability between two cell classes.

With this approach, we have accounted for distance dependence and functional connectivity between the different cell classes in our model. Our next step was to determine the dendritic targeting rules for the biophysically detailed model.

Dendritic Targeting for the Biophysical Model

The location of synapses between connected neurons has been demonstrated to have different patterns depending on the neuronal classes (Thomson and Lamy, 2007; Egger et al., 2015; Narayanan et al., 2015). Although, unfortunately, the available information is sparse, it does delineate trends that may be generalizable, and thus we used these data to implement the rules described below.

Excitatory-to-Excitatory Connections

All excitatory-to-excitatory connection avoided the soma and targeted the apical and basal dendrites. For layers 2/3, and 4, the connections were within 200 μm from the soma while for layers 5 and 6, the synapses could form anywhere along the dendrites (Thomson and Lamy, 2007; Egger et al., 2015; Narayanan et al., 2015). Note that the literature sources are mostly measurements from rat somatosensory cortex. The cortex depth in the rat is approximately 2 mm while our model it is 0.9 mm, and hence we scaled values accordingly.

Excitatory-to-Inhibitory Connections

For excitatory-to-inhibitory synapses, both the soma and dendrites could be targeted with no distance limitations (Thomson and Lamy, 2007). This was implemented for all layers and the values were again approximations from the relevant sources.

Inhibitory-to-Excitatory Connections (Inhibitory-to-Inhibitory Connections)

For inhibitory-to-excitatory connections we again depended on the data from rat cortex (Thomson and Lamy, 2007). Synapses from the Pvalb class were placed on the soma and dendrites within 50 μm from the soma of any target neuron. Synapses from Sst neurons were placed on the dendrites, 50 μm or further from the soma. Finally, synapses from Htr3a neurons were placed on the dendrites, from 50 μm to 300 μm from the soma. These rules also considered the morphology of neurons in the mouse visual cortex from reconstructions of axons and dendrites (Jiang et al., 2015). We assumed for these purposes that Pvalb neurons correspond to basket cells, Sst neurons to Martinotti cells, and Htr3a neurons to Bitufted and Bipolar cells described by Jiang et al. (2015).

Due to the lack of information on inhibitory-to-inhibitory connections, for this class of connections we used rules identical to the inhibitory-to-excitatory connections described above.

Layer 1

Finally, for layer 1 neurons, which are Htr3a only in our V1 model, we used the rules below that heavily depended on data from rat neocortex (Jiang et al., 2013) and neuron morphology from mouse V1 (Jiang et al., 2015), and are similar to other layers due to lack of references with explicit measurements. Our original goal for the model was to project i1Htr3a-to-E2/3 to apical dendrites (no somatic connections) from 50 μm and greater (see below). This is based on distance estimates from the bottom of L1 to upper L2/3 that are approximately 50 μm. This was decided by observing the extent of axonal arbors of L1 (according to Jiang et al., 2015, reconstructions). Similarly: i1Htr3a-to-E4 projected to apical dendrites that are 200 μm or further away from the soma; i1Htr3a-to-E5 projected to apical dendrites that are 300 μm or further away from the soma; i1Htr3a-to-E6 projected to apical dendrites that are 500 μm or further away from the soma; i1Htr3a-to-i1Htr3a projected everywhere including soma; i1Htr3a-to-i2/3 projected to basal dendrites from 50 μm and greater. For the other inhibitory layers that project to layer 1, the same rules were used as for within-layer i-to-Htr3a. Finally, excitatory projections to layer 1 were placed on the soma and dendrites with no distance limitations.

Note, however, that during our post-synaptic-potential optimization (see below), we had to change the rules of synaptic placement when L1 was the source onto excitatory cells. Our optimization methodology would create 100 target cells of a specific cell model that receive 1 spike at 0.5 s and we would record the generated postsynaptic potential (PSP). The weight would be scaled until we were within 1% of the target PSP. We observed that when L1 was the source impinging on excitatory cells, the targets sections were so far away for the somata of target cells residing in L4, L5, and L6, that the somatic PSP would reach a maximum and never match the target PSP regardless of how strongly the weight was scaled. This was due to the most distal compartments reaching their maximum membrane deviation that is equal to the reversal potential of the synaptic drive. With these distal compartments being at their maximum, and the attenuation that occurs due to dendritic filtering (recall dendrites in our model are passive), the soma would reach a maximum PSP that did not match our target values.

To address this issue, we changed the synaptic placement rules for L1-to-Excitatory neurons so that synapses were placed closer to the soma. In particular, the final rule used had all synapses placed at 50 μm or greater distance from the soma. In other words, all rules for L1-to-Excitatory synapse placement are identical to L1-to-E2/3 and drawn from a uniform distribution in the range [50 μm, dendrite length]. This is just a highly simplified approximation, but, in terms of reaching closer to the soma than our original rules, it is reasonable since L1 neurogliaform cells are known to bulk release GABA into large volumes and not form well-targeted synapses with post-synaptic cells (Szabadics et al., 2007; Oláh et al., 2009; Tremblay et al., 2016). In the future, employing neuronal models with active dendritic conductances will help alleviate such problems. While a number of such “all-active” biophysical neuronal models are already available in our Allen Cell Types Database (<http://celltypes.brain-map.org/>), they are much more computationally expensive than the “perisomatic” biophysical neuronal models with passive dendrites, used here. Furthermore, even the active dendrite models in the Allen Cell Types database have spatially uniform conductances, whereas to avoid the above described problem of distal inputs driving the dendritic voltage to synaptic reversal potential, one would have to include experimentally observed somatodendritic gradients of ion channels (leak, voltage-dependent potassium, HCN) to reduce the input impedance of small diameter dendritic branches. Developing reliable and accurate all-active neuronal models incorporating these gradients for a variety of cell types is thus an important avenue for future work.

Finally note that in our optimization we always let the cells relax to their baseline. Since the resting potential is lower than the reversal potential of the synapses, the single spike at 0.5 s would always cause a depolarization. We still used this depolarization level to optimize weights for excitatory PSPs and inhibitory PSPs.

Orientation Rule for Synaptic Strength

Matching Target Post Synaptic Potentials

The first version of our V1 model (Figures 4 and 5) used an orientation-dependent like-to-like rule for synaptic weights of all connection classes: E-to-E, E-to-I, I-to-E, and I-to-I (see Main Text). Since neurons had pre-assigned preferred angles, the connection strength was a function of the difference between the assigned angles of two connected neurons, defined within 90°. The synaptic strength between two cells was then defined as:

$$W = A_W e^{-\left(\frac{\Delta\theta}{\sigma_W}\right)^2}$$

where $\Delta\theta$ is the difference between the assigned angles of two neurons and σ_W is the standard deviation set to 50° for all connection classes. Finally, A_W is the weight constant that needed to be determined for every connection class to be matched to Post Synaptic Potential (PSP) targets.

For the biophysical model the units of W are in μS (defined as the peak conductance), and for GLIF model, in pA (see [Synaptic Characteristics](#)). Since most of the studies used to construct our PSP resource (Connection_strengths.pptx) employed *in vitro* patch-clamp experiments, the data do not distinguish a neuron’s functional preferences, such as preferred angle. Therefore, we assumed the neurons were targeted uniformly and, thus, for optimization we created 100 target cells from every model that were assigned tuning angles with equidistant spacing in the range [0, 360°]. We then created a virtual source node for every connection

class using the rules described above. The source node would emit 1 spike every 0.5 s. We then averaged the post-synaptic responses over all 100 target cells and iteratively updated the weight value (the factor A_W in the equation above) until the mean PSP was within 1% of the target value.

For scaling the weights when the target was a LIF neuron, 1000 source cells were created, each firing at 1Hz from a Poisson distribution. These cells would first target every *biophysical* cell model, using the synaptic weights that were already optimized as described above, and the resulting firing rates due to this input would be calculated. The target firing rate for the LIF neurons were then estimated as the weighted average rate (relative to the proportion of times a model would appear as part of a population). The same source cells (with identical spike times) would then be connected to LIF targets and the firing rate would be matched to within 5% of the desired firing rate.

For inhibitory connections onto the target LIFs, we used the same scaling factors as calculated for their excitatory counterparts. Although not ideal, we chose this route after checking our previous Layer 4 model (Arkhipov et al., 2018) and observing that indeed in that previous work the scaling ratios for LIFs for inhibitory input were approximately equal to the scaling ratios of excitatory inputs.

Finally, for the GLIF model, the weights could be calculated analytically based on connection strengths (i.e., PSPs) between the source and target populations (shown in Connection_strengths.pptx) and the mathematical model of the postsynaptic current (i.e., alpha function, see [Synaptic Characteristics](#)), together with the GLIF model membrane potential dynamics (Teeter et al., 2018). Namely, the weights were computed by solving the following equation that describe dynamics in the GLIF model after one spike injection.

$$\frac{\partial V(t)}{\partial t} = \frac{1}{C} \left(I_{syn}(t) - \frac{1}{R} (V(t) - E_L) \right)$$

where $V(t)$ is the membrane potential, C is the capacitance of the target neuron, $I_{syn}(t)$ is the alpha-shaped post-synaptic current function with weight W_{GLIF} (definition in [Synaptic Characteristics](#)), R is the resistance of the target neuron, and E_L is the resting potential. Note that weights in the GLIF model are current based while they are conductance based for the biophysical model. The steps for computing the weight W_{GLIF} based on the above GLIF model voltage dynamics are:

- 1) Solving the above dynamic equation to get the analytical solution of membrane potential $V(t)$;
- 2) Computing the derivative of the solution of $V(t)$, i.e., $\partial V(t)/\partial t$;
- 3) Setting $\partial V(t)/\partial t$ to zero and solving the equation to get the optimal time point t_{max} at which $V(t)$ reaches its maximum;
- 4) Substituting t_{max} for t and the target PSP for $V(t)$ to the solution of $V(t)$;
- 5) Solving the equation generated in 4) to get the weight W_{GLIF} .

The resultant solution for the weight W_{GLIF} is

$$W_{GLIF} = \begin{cases} V_{target} C \left(\frac{1}{\tau_m} - \frac{1}{\tau_{syn}} \right) e^{\frac{1}{\left(\frac{1}{\tau_m} - \frac{1}{\tau_{syn}} \right) \tau_{syn}}} & \tau_m \neq \tau_{syn} \\ \frac{V_{target} C e^1}{2 \tau_m} & \tau_m = \tau_{syn} \end{cases}$$

with V_{target} being the target PSP, τ_{syn} being the synapse time constant, and τ_m being the membrane time constant.

Optimization of Full V1 Models

As described in the Main Text, running simulations after the above optimization did not yield suitable network behaviors in either of our V1 models. Thus, we used an iterative grid search method (Arkhipov et al., 2018), where weights were uniformly scaled for every class (e.g., scaling weights of excitatory layer 4 to excitatory layer 5 connections all by the same amount, as one iteration). We searched in discrete increments weight changes across connection classes and selected the best result before moving on to the next connection class (although there was still a need to revisit connections classes during this process). The optimization employed a small training set consisting of two 0.5 s-long simulations: one of gray screen, and the other of a single drifting grating. We aimed to satisfy three criteria: (i) match spontaneous firing rates (gray screen stimulus) to experimental observations, (ii) match peak firing rates for the drifting grating, and (iii) avoid epileptic-like activity where the network would ramp up to have large global bursts and then enter a period of silence until the next very rapid burst. The weight adjustments were kept in a strict range where, for example, the LGN to L4 excitatory weights were not adjusted at all given that they were fit to direct *in vivo* experimental measurements (Lien and Scanziani, 2013). Other LGN connections were restricted to be scaled only in the range [0.5, 2] from the target net input current as those were scaled from optogenetics experiments (Ji et al., 2016). The optimization was performed starting from L4 only and adding successive layers one by one (Figures 4G and S3). First, all interlayer connections were set to zero and only the intra-layer connections in L4 were optimized. Once our criteria were met, we added L2/3 to the optimization, including the interactions between the two layers. This procedure simplified the optimization process even though weights optimized at one step had to be readjusted at the next step (typically minor). This process was continued for layer 5, followed by layer 6, and finally layer 1. During our optimization, the weight scaling was restricted in the range of [0.2, 5]. In the deeper layers (layers 5 and 6), this rule had to be expanded to reach the net adjustment

range of [0.12, 18] for the biophysical model and [0.17, 6.0] for the GLIF model. Note that adjusting the synaptic weights in the biophysical model did not translate directly to scaling the PSP (see the Layer 1 description in [Dendritic Targeting for the Biophysical Model](#)). The order of adding layers was selected based on the canonical cortical microcircuit ([Douglas et al., 1989, 1995; Douglas and Martin, 2007](#)). We expect that using such biological insights to guide optimizations of large-scale biological models, perhaps as a strategy accompanying algorithmic methods, may increase the speed and likelihood of convergence.

Optimization with the Direction-Based Rule and Phase Dependence for Synaptic Strength

As described in the Main Text, the next version of our V1 models used a rule for synaptic strengths that was asymmetric with respect to the reversal of direction and included phase dependence, such that the strongest synaptic inputs were sourced from a stripe perpendicular to the preferred direction of the target cell ([Figures 6A and 6B](#)). Once this rule was introduced, the weights needed to be optimized further, as the balance in the network was affected. As a first step, we scaled the recurrent synaptic weights so that the net current (area under the curve, [Figure 6A](#)) became the same as in the previous version of the model ([Figure 4D](#)) for every connection class. However, this was not sufficient, and, thus, we further performed another round of optimization as described in the above section. It turned out that because of the scaling to match the area under the curve, the weights were already close to the correct solution, and we found that these new optimizations required only a few iterations before converging to meet our criteria. For the same reason, here it was not necessary to optimize the models layer-by-layer, and instead the optimization was performed with the full recurrent connectivity. The weight scaling was not constrained to tight limits, however, due to the new synaptic strength profiles that deviated substantially and in a non-linear fashion from those used before.

Correcting for Biases between Horizontal- and Vertical-Preferring Neurons

After finalizing the optimization using the rules above, we noticed biased firing rates in our models, in that vertical drifting gratings evoked higher firing rate relative to horizontal gratings ([Figure 6C](#)). Since this was not observed experimentally and was a result of extra excitatory synaptic drive into vertically preferring neurons ([Figure S6](#)), we adjusted incoming synaptic weights to maintain equal net synaptic drive. The adjustment depends on the cortical magnification factors in the azimuth and elevation dimensions. As described in [Visual Coordinates](#), the physical dimensions of each V1 neuron was converted to visual space by a conversion factor of 70 degrees/mm in the azimuth (x-dimension) and 40 degrees/mm in elevation (z-dimension), estimated from experimental reports ([Schuett et al., 2002; Kalatsky and Stryker, 2003](#)). To adjust for this asymmetry, we collapsed every neuron's preferred angle to the quadrant $\theta = [0, 90]$ and scaled synapses to neurons that preferred horizontal motion (0-degrees) by

$$\frac{(70+40)/2}{40} = \frac{5.5}{4}$$

whereas synapses to neurons preferring vertical motion (90-degrees) were scaled by:

$$\frac{(70+40)/2}{70} = \frac{5.5}{7}$$

Given these two points, we then fit a linear function to estimate the weight scaling for every intermediate value, resulting in

$$W_{\text{factor}} = \frac{5.5}{4} - \frac{11}{1680} \times \theta$$

This weight adjustment fixed the bias ([Figures 6C and S6](#)) and resulted in horizontal-preferring neurons having a heavier tail of the incoming synaptic strength distribution than vertical-preferring neurons ([Figure 6E](#)). Finally, due to our highly non-linear V1 models, this adjustment resulted in deviations from our target optimization firing rates. Thus, a small amount of grid search tuning was needed again to match our target criteria.

Synaptic Characteristics

The synaptic mechanisms used for the biophysical model were as in the L4 model ([Arkhipov et al., 2018](#)). The synapses were bi-exponential (using NEURON's Exp2Syn mechanism) with a reversal potential of -70 mV for inhibition and 0 mV for excitation. The weights' units are in μS (peak conductance). The tau1 and tau2 constants for the mechanism were 2.7 ms and 15 ms for inhibitory-to-excitatory synapses, 0.2 and 8 ms for inhibitory-to-inhibitory synapses, 0.1 ms and 0.5 ms for excitatory-to-inhibitory synapses, and 1 ms and 3 ms for excitatory-to-excitatory connections. Note that these are not the somatic temporal characteristics, but time constants at the synaptic location; the PSP shape at the soma depends on dendritic location of the synapse and membrane dynamics.

For the GLIF model, postsynaptic current-based synaptic mechanisms were used with dynamics described by an alpha-function:

$$I_{\text{syn}}(t) = \frac{eW_{\text{GLIF}}}{\tau_{\text{syn}}} t e^{-\frac{t}{\tau_{\text{syn}}}}$$

Where I_{syn} is the postsynaptic current, τ_{syn} is the synaptic port time constant, and W_{GLIF} is the input connection weight. This function was normalized such that a post-synaptic current with synapse weight $W_{\text{GLIF}} = 1.0$ has an amplitude of 1.0 pA at the peak time point of $t = \tau_{\text{syn}}$. The τ_{syn} constants for the mechanisms were 5.5 ms for excitatory-to-excitatory synapses, 8.5 ms for inhibitory-to-excitatory synapses, 2.8 ms for excitatory-to-inhibitory synapses, and 5.8 ms for inhibitory-to-inhibitory connections, which were extracted from LIF models in the L4 model ([Figure S2B of Arkhipov et al., 2018](#)).

Visual Stimuli

The visual stimuli used in our simulations were identical to those used for the experiments we compare to (except the looming disk that had no experimental counterpart). Each simulation included a 500 ms interval of gray screen in the beginning, which was then followed by a single trial of presentation of the stimulus.

Drifting Gratings

For the drifting grating stimuli, we used sinusoidal gratings with a spatial frequency of 0.04 cycles per degree with a temporal frequency of 2Hz (for 2.5 s after the gray-screen). All stimuli were run for 10 trials for every direction of motion (8 sampled directions with increments of 45 degrees) at 80% contrast (for both the experiments and the models). Although the experimental data from mice (see below) included more temporal and spatial frequencies, we restricted our analysis to match the drifting gratings used in our simulations.

Flashes

The flash stimuli (10 trials) consisted of: 500 ms of gray screen, followed by 250 ms of white screen (ON-flash), returning to a gray screen for 1000 ms, then another 250 ms of black screen (OFF-flash), and a final gray screen for 500 ms). The contrast was at 80% (to match experiments). We also conducted simulations with full-contrast flashes (100%), and the models were stable and produced results very similar to the 80% contrast case (data not shown).

Natural Movies

We tested our models on a clip (10 trials) from one of the natural movies (*Touch of Evil*, directed by Orson Welles) used in the Allen Brain Observatory (de Vries et al., 2020). The 2.5 s shown were matched between the model and experiment.

Looming Disk

The looming stimulus is a growing black disk (circle) on a gray background. When the maximum circle size (radius of 25 degrees) is reached, the circle disappears and grows again. This is repeated four times throughout the 2.5 s stimulus presentation (625 ms duration for every repetition).

Electrophysiological Recordings**Animal preparation**

All experimental procedures were approved by the Allen Institute for Brain Science Institutional Animal Care and Use Committee. Five weeks prior to the experiment, mice were anesthetized with isoflurane, and a metal headframe with a 10-mm circular opening was attached to the skull with Metabond. In the same procedure, a 5-mm-diameter craniotomy and durotomy was drilled over left visual cortex and sealed with a circular glass coverslip. Following a 2-week recovery period, a visual area map was obtained through intrinsic signal imaging (Juavinett et al., 2017). Mice with well-defined visual area maps were gradually acclimated to the experimental rig over the course of 12 habituation sessions. On the day of the experiment, the mouse was placed under light isoflurane anesthesia for ~40 min to remove the glass window, which was replaced with a 0.5 mm thick plastic window with laser-cut holes (Ponoko, Inc., Oakland, CA). The space beneath the window was filled with agarose to stabilize the brain and provide a conductive path to the silver ground wire attached to the headpost. Any exposed agarose was covered with 10,000 cSt silicone oil, to prevent drying. Following a 1-2 hour recovery period, the mouse was head-fixed on the experimental rig. Up to six Neuropixels probes coated in CM-Dil were independently lowered through the holes in the plastic window and into visual cortex at a rate of 200 $\mu\text{m}/\text{min}$ using a piezo-driven microstage (New Scale Technologies, Victor, NY). When the probes reached their final depths of 2,500–3,500 μm , each probe extended through visual cortex into hippocampus and thalamus. Only data obtained from V1 was included in this study. In total, data from 20 mice were used for the drifting gratings analysis (one experiment per mouse) and 7 mice for the natural movie and flash analysis.

Data acquisition system

Recordings were performed in awake, head-fixed mice allowed to run freely on a rotating disk. During the recordings, the mice passively viewed a battery of visual stimuli, including local drifting gratings (for receptive field mapping), full-field flashes, drifting gratings, static gratings, natural images, and natural movies, with the same parameters as those from the Allen Brain Observatory (de Vries et al., 2020). All spike data were acquired with Neuropixels probes (Jun et al., 2017) with a 30-kHz sampling rate and recorded with the Open Ephys GUI (Siegle et al., 2017). A 300-Hz analog high-pass filter was present in the Neuropixels probe, and a digital 300-Hz high-pass filter (3rd-order Butterworth) was applied offline prior to spike sorting.

Data preprocessing

Spike times and waveforms were automatically extracted from the raw data using Kilosort2 (<https://github.com/mouseland/kilosort2>). Kilosort2 is a spike-sorting algorithm developed for electrophysiological data recorded by hundreds of channels simultaneously. It implements an integrated template matching framework for detecting and clustering spikes, rather than clustering based on spike features, which is commonly used by other spike-sorting techniques. After filtering out units with “noise” waveforms using a random forest classifier trained on manually annotated data, all remaining units were packaged into Neurodata Without Borders format (Teeters et al., 2015) for further analysis.

Neuronal Classification

Regular spiking (RS) neurons and fast spiking (FS) neurons were determined by the duration of the spike (time between trough and peak of the waveform). The duration of the spikes showed a bimodal distribution (Hartigan dip test, $p = 0.004$), with a dip at 0.4 ms. We classified a neuron as RS if its duration was > 0.4 ms, and otherwise FS (Figure S2). In total we had 328 L6 RS neurons, 72 L6 FS

neurons, 419 L5 RS neurons, 80 L5 FS neurons, 294 L4 RS neurons, 49 L4 FS neurons, 251 L23 RS neurons, 49 L23 FS neurons, and 81 L1 neurons.

QUANTIFICATION AND STATISTICAL ANALYSIS

Firing Rates

The firing rates were estimated from all trials of a simulation. Since all simulations started with a 500ms gray-screen period followed by the stimulus, the firing rate is estimated using the stimulus duration without these first 500 ms (that is, 2500 ms for a drifting grating or a natural movie). Thus, the firing rate for a neuron in a trial was calculated by dividing the total number of spikes after the gray screen by the stimulus duration (2500 ms). Some metrics required time-dependent firing rates that are described below. For the OSI and DSI metrics, to avoid noise from very sparsely firing neurons that could yield spurious OSI/DSI values of 1.0, we required that neurons' firing rates at their preferred drifting grating direction be greater than 0.5 Hz. Further, for the OSI and DSI metrics, the firing rates were normalized by their own spontaneous baseline firing rate (average firing rate of a neuron in the gray screen period over 80 trials). In addition, we calculated the rates in the interval [50, 500] ms after stimulus onset as done experimentally.

Orientation Selectivity Index (OSI)

The OSI metric computed is also referred to as the global Orientation Selectivity Index, as it takes into account the response of a neuron in all directions tested (not just the preferred and orthogonal). The OSI is calculated as:

$$OSI = \frac{|\sum R_\theta e^{2i\theta}|}{\sum R_\theta}$$

where R_θ is the mean firing rate response to a drifting grating of angle θ .

Direction Selectivity Index (DSI)

Similar to the OSI metric, the DSI also considered responses in all directions of drifting gratings shown (sometimes referred to as the global Direction Selectivity Index). The DSI is calculated as:

$$DSI = \frac{|\sum R_\theta e^{i\theta}|}{\sum R_\theta}$$

where R_θ is the mean firing rate response to a drifting grating of angle θ .

Response at Preferred Direction

The plots quantifying neurons' response at their preferred direction report the mean firing rate values based on the largest mean response (across trials) over all 8 directions tested.

Signal Correlations, Noise Correlations, and Correlation of Signal and Noise Correlations

We computed the signal correlation as the Pearson correlation coefficient between the trial-averaged spike counts for each pair of neurons (Arkhipov et al., 2018). For natural movies, we computed the correlation for binned spike counts in non-overlapping windows of length 50 ms. For gratings, the correlation was computed over the spike counts in 8 different directions. The noise correlation was computed as the Pearson correlation coefficient between single-trial spike counts for each pair of neurons, and then averaged over stimuli conditions (8 directions for gratings and non-overlapping 50 ms windows for natural movies). To compute the correlation of signal and noise correlations for a single experimental mouse, we calculate the Pearson correlation coefficient between the noise correlation and signal correlation metrics already calculated. Since we have many mice (20 for drifting gratings, 7 for natural movies), we subsample neurons within 150 μ m from the center mini-column of the models to match the number of neurons per mouse. The subsampling is without replacement. We restricted the sampling near the center of the models to match experimental Neuropixels recording as much as possible.

Lifetime and Population Sparsity

Lifetime sparsity for each neuron was computed using the following definition (Vinje and Gallant, 2000):

$$S_L = \frac{1 - \frac{1}{N} \frac{(\sum_i r_i)^2}{\sum_i r_i^2}}{1 - \frac{1}{N}}$$

where N is the number of stimulus conditions and r_i is the trial-averaged spike count for stimulus condition i (de Vries et al., 2020). To compute the population sparsity, we used the same equation, but where N is the total number of neurons in the population and r_i is the average spike-count of neuron i over all stimulus conditions (de Vries et al., 2020).

Similarity Score

A similarity score was developed to compare the distribution of all excitatory neurons in the models with all regular spiking neurons recorded experimentally as well as for Pvalb neurons in the models with fast-spiking neurons from the same Neuropixels recording. The score compares any two distributions and does not require a normality assumption nor that both distributions have an equal number of samples. Moreover it can be applied to any metric and we use it here to compare OSI, DSI, and the firing rate distributions of the models with experiments. The metric uses the D statistic from a Kolmogorov–Smirnov test that calculates the distance between the cumulative distributions of two samples and is bounded in the range [0, 1]. Since we are interested in similarity in this work and matching distributions, this was converted to a similarity score, $S = 1 - D$. Figure S2F illustrates how for two different distributions S is close to 0, whereas for two similar distributions it approaches 1.

DATA AND CODE AVAILABILITY

The models and code generated during this study are available at <https://portal.brain-map.org/explore/models/mv1-all-layers>.

ADDITIONAL RESOURCES

The experimental data is available publicly at <https://portal.brain-map.org/explore/circuits/visual-coding-neuropixels>.